

Neotectonic faults in the Southern Chile intra-arc (38°S–40.5°S): Insights about their seismic potential and the link with the megathrust earthquake cycle

Luis Astudillo-Sotomayor^{a,b,h}, Joaquín Cortés-Aranda^{a,b,*}, Daniel Melnick^{b,c}, Julius Jara-Muñoz^d, Catalina Cabello^{a,b}, Laura Perucca^e, Andrés Tassara^{a,b}, José Vicente Pérez-Peña^f, Pablo León-Ibáñez^g

^a Departamento de Ciencias de la Tierra, Universidad de Concepción, Concepción, Chile

^b Millennium Nucleus the Seismic Cycle Along Subduction Zones, Valdivia, Chile

^c Instituto de Ciencias de la Tierra, TAQUACH, Universidad Austral de Chile, Valdivia, Chile

^d Faculty of Civil Engineering, Hochschule Biberach, 88400, Biberach an der Riß, Germany

^e Instituto de Geología (INGEO), Universidad Nacional de San Juan-CONICET, Argentina

^f Departamento de Geodinámica, Universidad de Granada, Campus de Fuentenueva, 18071 Granada, Spain

^g Departamento de Geología, Facultad de Ciencias Físicas y Matemáticas, Universidad de Chile, Santiago, Chile

^h Facultad de Ingeniería, Universidad Andrés Bello, Concepción, Chile

ARTICLE INFO

Keywords:

Liquiñe-Ofqui Fault System
Quaternary fault activity
Strain partitioning
Coulomb failure stress change

ABSTRACT

Megathrust earthquakes are a primary geological hazard in subduction zones. In oblique subduction margins, however, seismic threat must be also considered concerning crustal strike-slip faults driving the parallel-to-the-trench component of the convergent vector. These faults have proven their capacity to produce moderate-to-large shallow earthquakes, causing severe damage for surrounding areas. The Southern Chile Subduction Zone (SCSZ) is characterized by the oblique convergence between the Nazca and the South America plates. Between 37°S and 46°S, slip partitioning is significantly led by intra-arc faults like the Liquiñe-Ofqui Fault System (LOFS) and subsidiary NW to NE striking structures. Despite it has been demonstrated that the behavior of these faults is seismogenic, the inland evidence of Holocene deformation along them is scarce. This has concealed to accurately define individual active faults, discussing their seismic potential, and addressing their link with the megathrust earthquake cycle. In this contribution, we first present field evidence for Holocene deformation on intra-arc faults in the area. Based on this, we define 5 active faults and discuss their seismic capacity. To assess the link with the megathrust earthquake cycle, we calculate the Coulomb stress changes induced on these faults by the Mw 9.5 Valdivia Earthquake slip distribution and an interseismic period of 300 years. We conclude that 1) the identified neotectonic faults have the potential for producing moderate-to-large earthquakes (Mw 5.5 to 6.8) and 2) their occurrence would be enhanced by the coseismic and the interseismic stages of the subduction cycle. With this, we propose that the intra-arc faults addressed in this paper, and certainly others in the SCSZ, must be considered as significant sources of seismic hazard.

1. Introduction

In oblique convergent tectonic settings, slip partitioning between the megathrust and strike-slip upper-plate fault systems is a common process (Allen, 1965; Fitch, 1972). Crustal strike-slip faults in these environments, in several cases, have proven their potential for producing moderate-to-major (Mw 5–7.9) earthquakes (e.g., Nakano et al.,

2010). The occurrence of these shallow crustal earthquakes has been related to triggering by stress perturbations induced by the megathrust earthquake cycle (Bufe, 2006; McCloskey et al., 2005; Mitogawa and Nishimura, 2020). Strike-slip fault reactivation in oblique subduction zones has been reported decades after megathrust earthquakes, for instance, in Japan (M 7.1995 Kobe Earthquake; Pollitz and Sacks, 1997) and Alaska (M 7.92022 Denali Earthquake; Bufe, 2006). This evidence

* Corresponding author at: Millennium Nucleus the Seismic Cycle Along Subduction Zones, Valdivia, Chile.

E-mail address: joacortes@udec.cl (J. Cortés-Aranda).

<https://doi.org/10.1016/j.tecto.2022.229675>

Received 29 March 2022; Received in revised form 30 November 2022; Accepted 2 December 2022

Available online 9 December 2022

0040-1951/© 2022 Elsevier B.V. All rights reserved.

indicates that, in oblique subduction zones, earthquake hazard must not only be addressed concerning the megathrust but also regarding upper plate strike-slip faults driving slip partitioning (e.g., Bellier et al., 1997).

At the Southern Chile subduction zone, between 37°S and 46°S, the dextral-oblique convergence between the Nazca and South America plates is significantly partitioned (Cembrano et al., 2002). There, the Liquiñe-Ofqui Fault System (LOFS), a dextral-transpressive intra-arc structure (Lavenue and Cembrano, 1999), partially accommodates the

trench-parallel component of the convergence vector (Rosenau et al., 2006; Stanton-Yonge et al., 2016; Wang et al., 2007); this is facilitated by the thermally weakened crust of the volcanic arc (Cembrano et al., 1996, 2000; Cembrano and Lara, 2009). The instrumental evidence attests for the seismogenic behavior of this structure. Shallow (<15 depth) microseismicity ($M_w < 4$) and shallow moderate-to-large ($M > 6$) earthquakes have been recorded along the LOFS and spatially related faults (Legrand et al., 2011; Pérez-Estay et al., 2020; Sielfeld et al.,

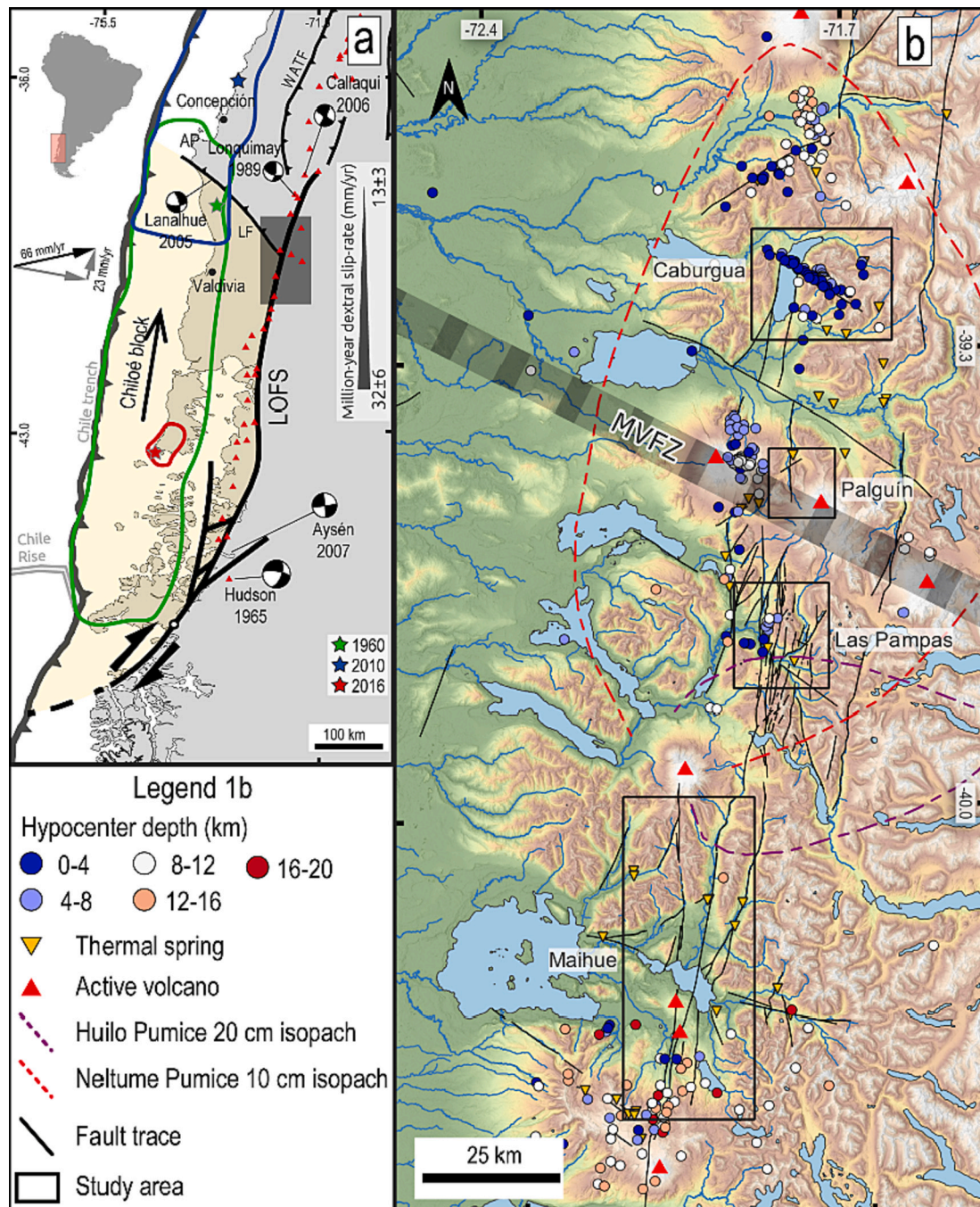


Fig. 1. a) Seismotectonic setting of the Patagonian Andes. Focal mechanisms of major earthquakes along the Liquiñe-Ofqui Fault System (LOFS) and Llanquihue Fault (LF) from CMT Catalog, (Pérez-Flores et al., 2016) and (Haberland et al., 2006). Black and grey arrows depict Nazca-South American plate convergence vector (Angermann et al., 1999) and decomposed components, respectively. Colored stars indicate the epicenter of major megathrust earthquakes within the Valdivia and Constitución segments; Green: Valdivia 1960; blue: Maule 2010, red: Melinka 2016. Colored lines correspond to the rupture area of the aforementioned earthquakes (Moreno et al., 2018; Moreno et al., 2009; Tong et al., 2018). Regional faults from (Melnick et al., 2009). AP: Arauco Peninsula. Million-year scale dextral slip rate for the LOFS from Rosenau et al. (2006) kinematic model. Grey shaded area corresponds to the area shown in b. b) Map of the studied area. Crustal faults from Maldonado et al. (2021). Neltume and Huilo isopach contours from Rawson et al. (2015). Crustal seismicity from Sielfeld et al. (2019) and IRIS catalog (<https://www.iris.edu/hq/>). (For interpretation of the references to colour in this figure legend, the reader is referred to the web version of this article.)

2019). Despite this, the reported inland evidence for past (Late Quaternary) earthquakes is scarce, due to a combination of factors such as preservation issues (related to the action of surface and volcanic processes), the dense vegetation cover, and the difficulty to access to remote areas where LOFS branches run; this has significantly concealed the accurate identification of individual neotectonic intra-arc faults, discussing their seismogenic potential, and their link with the megathrust earthquake cycle.

In this contribution, we present evidence for inland Late Quaternary deformation produced by faults in the Chilean intra-arc between 39°S and 40.5°S (Fig. 1b). In general, the evidence consists of deflected channels and offset markers at the 10–10² m scale; these observations were carried in four areas (black rectangles in Fig. 1b). Based on the presented evidence, we define individual neotectonic intra-arc faults and discuss their earthquake potential. To assess whether the activity along these faults may be enhanced to slip during the interseismic and/or coseismic stages of the megathrust earthquake cycle, we use Coulomb Failure Stress changes (Δ CFS) models. The aim of this contribution is to assess the seismic hazard potential in the Chilean intra-arc region between 39°S and 40.5°S, which is important considering the presence of several urban areas and strategical facilities that can be severely affected by moderate-to-large earthquakes on faults located in the area.

2. Geological framework

2.1. Tectonic and seismotectonic setting (38°S–47°S)

The convergence between the South American and Nazca plates is the leading process regarding the tectonic configuration of Southern Chile (Fig. 1a). This process has acted at a roughly constant velocity and oblique to the margin since the Miocene (Quiro et al., 2022), preceded by a period of orthogonal convergence during the Miocene (Maloney et al., 2013; Pardo-Casas and Molnar, 1987). Nowadays, convergence occurs at a rate of 66 mm/yr, with an obliquity of 26° (Angermann et al., 1999; Jarrard, 1986; Kendrick et al., 2003; Kendrick et al., 1999). In the study area, the convergence-induced deformation is highly partitioned between the megathrust, the LOFS, and Andean Transverse Faults (ATFs; Pérez-Flores et al., 2016).

The south-central Chilean subduction margin has been struck by several moderate-to-great earthquakes during the last centuries, allowing the delineation of two major seismotectonic segments: the Constitución and Valdivia segments (Lomnitz, 2004). The Valdivia segment was breached by the Mw 9.5 Valdivia 1960 earthquake, the largest recorded seismic event. This earthquake ruptured ~1000 km, roughly encompassing the length of the LOFS (Fig. 1); it slipped the shallower portion of the interplate contact, involving an average slip of 17 m and a local maximum slip of 44 m (Barrientos and Ward, 1990; Fujii and Satake, 2013; Moreno et al., 2009). During the decades after the earthquake, a protracted postseismic rebound of the mantle dominated the 1960s rupture region (Khazaradze et al., 2002). According to Melnick et al. (2018), the Valdivia segment was seismically quiet after the 1960 earthquake; since then, the interseismic interplate locking has been heterogeneous, with highly locked patches separated by creeping areas. In 2016, the Mw 7.6 Melinka earthquake broke the deeper portion of a single highly locked patch of the seismogenic zone beneath the southern coast of Chiloé Island, at the southern extent of the Valdivia rupture zone (Fig. 1a; Melnick et al., 2018). Slip solutions for this event suggest a single rupture with a maximum slip of 2.9 m, which represents ~80% of the slip deficit accumulated between 1960 and 2016 (Moreno et al., 2018). The Melinka earthquake is the first event on the Valdivia segment after the 1960 Valdivia earthquake, suggesting the seismic reactivation of this portion of the Chilean megathrust (Lange et al., 2018).

2.2. Structural synthesis

The LOFS (Fig. 1a) is the main structural feature of the intra-arc in the Southern Volcanic Zone (SVZ); it corresponds to a 1200 km-long dextral-transpressive fault system with secondary NE-ESE-trending structures (Cembrano et al., 1996, 2000). This structure favors the decoupling and northward translation of a forearc sliver, the Chiloé Block (Forsythe and Nelson, 1985). At a regional scale, the LOFS consists of NNE-striking dextral strike-slip faults strands; NE-striking normal-dextral faults splay off the main NNE strands, defining duplexes and horsetails at the northern and southern tips of the system (Fig. 1a). The LOFS is spatially associated with major stratovolcanoes, ENE-oriented volcanic lineaments, subparallel diking, and hydrothermal centers (Cembrano et al., 2000; Cembrano and Lara, 2009; Lara et al., 2008; Melnick et al., 2006a, Melnick et al., 2006b; Pérez-Flores et al., 2016, 2017; Rosenau et al., 2006; Sánchez et al., 2013; Sielfeld et al., 2017).

Between 6 and 3 Ma, the LOFS has accommodated dextral ductile deformation (e.g., Cembrano et al., 2000); then, since 1.6 Ma, this structure has led dextral brittle deformation (e.g., Lavenue and Cembrano, 1999). Deformation rates for the LOFS have been constrained both for the long-term and instantaneous timespans. Based on kinematic models, Rosenau et al. (2006) obtain mean shear rates decreasing northwards from 32 ± 6 mm/yr to 13 ± 3 mm/yr for the last 4 Ma (Fig. 1a). Present-day GPS velocities show northward motion of the Chiloé Block, driven by dextral shear along the LOFS at northward decreasing rates of 6.5 mm/yr (Wang et al., 2007). Further, boundary element models suggest a 3.5 mm/yr slip rate for the LOFS Eastern Master Fault and a 5 mm/yr slip rate for the Western Master Fault (Stanton-Yonge et al., 2016). In turn, finite element models propose a northward increasing from 7 to 10 mm/yr slip rates for the Eastern Master Fault and a northward decreasing from 1 to 4 mm/yr slip rates for the Western Master Fault (Iturrieta et al., 2017). Despite the documentation of Late Quaternary deformation evidence (subaerial and subaqueous) for the LOFS (Melnick et al., 2006a, Melnick et al., 2006b; Vargas Easton et al., 2013; Villalobos et al., 2020; Wils et al., 2018, 2020), the estimation of millennial slip rates has remained elusive. Recently, Astudillo-Sotomayor et al. (2021) estimated a dextral slip-rate of 18.8 ± 2.0 mm/yr for an individual major branch of the LOFS for the last 9 ky, by considering deformed fluvial terraces near the Liquiñe village. The authors also suggest that, at the millennial timescale, slip partitioning between the megathrust and the LOFS is high, and that strain concentrates on a single LOFS strand during this time span. Further south, near the Huemules River (~45.83°S), De Pascale et al. (2021) suggest a Quaternary 11 to 24 mm/yr dextral slip rate for a LOFS master fault, based on displaced glacial landforms. However, these glacial landforms have not been yet dated and therefore these rates remain speculative.

Seismic activity has been recognized throughout the LOFS (Fig. 1). Instrumental data shows the occurrence of clusters of shallow micro-seismicity reaching depths up to 12 km, which are regarded as the seismogenic layer bottom (Fig. 1b; Pérez-Estey et al., 2020; Sielfeld et al., 2019). The oldest Mw ≥ 5 recorded event within the LOFS is the Mw 6.21964 Hudson earthquake; this event occurred at 11 km depth along a NE-striking fault (Chinn and Isacks, 1983). In 1989, a Mw 5.3 earthquake took place shortly after an eruption of the Lonquimay Volcano; this event occurred at 15 km depth and involved dextral-oblique slip on a NNE-striking fault (Fig. 1a; Barrientos et al., 1992). In 2006, a Mw 5.5 earthquake at 18 km depth occurred at the northern end of the LOFS, nearby the Callaqui Volcano; the constrained focal mechanism suggests either dextral slip on a NNE-striking fault or sinistral slip on a NW-striking fault; both fault styles occur in the area (Fig. 1a; Pérez-Flores et al., 2016). In 2007, a seismic swarm occurred along the LOFS at the Aysén fjord, ending with an Mw 6.2 earthquake at 12 km depth; the focal mechanism for this event was right-lateral with slip on a NS-striking plane (Fig. 1a; Legrand et al., 2011).

The intra-arc area is also characterized by a system of NW-striking

faults defined as Andean Transverse Faults (ATFs), which are regarded as pre-Andean inherited structures (Haberland et al., 2006; Lange et al., 2008; Lara et al., 2006; Melnick et al., 2006a, Melnick et al., 2006b; Melnick and Echtler, 2006). These faults have been considered as lithospheric deep-rooted structures based on geophysical evidence, field observations, and remote sensing (Sánchez et al., 2013). The ATFs are spatially related to the development of Cenozoic basins (Radic, 2010), the segmentation of the megathrust rupture zones (Melnick et al., 2009), and the Quaternary volcanism in the Southern Volcanic Zone (SVZ; Cembrano and Lara, 2009). In addition, the ATFs partially control fluid circulation and have been associated to shallow seismicity (Cembrano and Lara, 2009; Lara et al., 2006; Melnick et al., 2006a, Melnick et al., 2006b; Pérez-Flores et al., 2016; Sielfeld et al., 2017; Tardani et al., 2016).

3. Methods

3.1. Characterization of the neotectonic evidence

Four areas with neotectonic evidence are herein reported for the Southern Chile intra-arc between 39°S and 40.5°S. These areas, from north to south, were named Caburgua, Palguín, Las Pampas and Maihue (areas in Fig. 1b). The definition of these areas was primarily led by a detailed literature review including published and unpublished studies. For each area, key sites were then confirmed after a first field survey. The evidence preserved in these specific sites corresponds to offset landforms and faulted Quaternary deposits. Then, specific sites were characterized based on high-resolution satellite imagery (Landsat/Copernicus data from Google Earth) and ALOS-PALSAR Digital Elevation Models (DEMs) with 12.5 m spatial resolution analysis. During a second field survey, work focused on mapping, describing, and analyzing neotectonic evidence of fault activity in each site from geomorphic, stratigraphical, and structural standpoints. These tasks pointed to interpret the evidence in terms of fault kinematics and its neotectonic significance. The description of most of the sites was supported by drone imagery and high-resolution topography derived from photogrammetry. For those sites where the first-order evidence is given by deformed channels, offset estimations were undertaken on high-resolution DEMs considering the approach of Zielke and Arrowsmith (2012).

To constrain the timing of deformation, we have first considered the age of the deposits presented in published geological charts of the area; these mostly correspond to lacustrine, fluvial, pyroclastic, glacial, and undifferentiated deposits (Campos et al., 1998; Moreno Roa and Lara, 2008; Rawson et al., 2015). Then, when possible, charcoal fragments were collected from buried soils to obtain radiocarbon ages. Further, pumice samples were collected at some sites to perform correlations with a tephrochronological database for the Chilean lake district (Rawson et al., 2015); the major oxide composition of the glassy matrix of the pumice samples was analyzed by using a JEOL JXA-8200 wavelength dispersive electron microprobe equipped with five spectrometers at the Institute of Geosciences, Potsdam University.

At the Palguín Area, a GPR profile was carried out with a GSSI UtilityScan equipment (<https://www.geophysical.com/products/utilityscan>). The obtained data were later processed using the RADAN 7 software (<https://www.geophysical.com/software>). This allowed imaging strata and structures at depth (Fig. 6g–i). Unfortunately, due to access difficulties and water oversaturation of the deposits, this technique was not employed in the other 3 areas.

3.2. ΔCFS models

The static Coulomb Failure Stress change (ΔCFS) analysis has been widely implemented to quantitatively evaluate the influence of the megathrust earthquake cycle on crustal faults (e.g., Aron et al., 2013; Farías et al., 2011; Loveless et al., 2010; Sgambato et al., 2020). The

ΔCFS is defined as:

$$\Delta\sigma_c = \Delta\tau + \mu' \Delta\sigma_n$$

where $\Delta\tau$ is the shear stress change (positive in the direction of receiver fault slip), $\Delta\sigma_n$ is normal stress change (positive when the receiver fault is unclamped), and μ' is the effective fault friction coefficient on the receiver fault (considering pore pressure).

For our modeling, we have employed the Coulomb 3.4 software (Toda et al., 2011). We calculated ΔCFS for “Optimally Oriented Faults” (OOFs) – thrust (rake 90°), normal (rake –90°), and dextral strike-slip faults (rake 180°) – considering a grid of 5 by 5 km. The OOFs are those faults along which the ΔCFS is maximum, thus the more likely to slip. The dipping angle for the dip slip faults is controlled by the coefficient of friction (μ) as follows:

$$\beta = \frac{1}{2} \tan^{-1} \left(\frac{1}{\mu} \right)$$

with β being the dip angle for reverse faults and the $(90-\beta)$ the dip of the normal faults. Strike-slip faults are considered as vertical structures (Toda et al., 2011).

For our modeling approach, we have considered two interplate scenarios; first, we model the ΔCFS induced by the coseismic slip of the Mw 9.51960 Valdivia Earthquake considering the slip distribution of Fujii and Satake (2013) (Fig. S4a). Second, we model the ΔCFS induced by the “backslip” (e.g., Savage, 1983) – considering the modern interseismic locking from Moreno et al. (2011) (Fig. S4b) – for simulating the interseismic slip deficit accumulated during 300 yr (Fig. S4c), which is the proposed recurrence time for Valdivia type earthquakes (Cisternas et al., 2005). To discuss in which degree the herein characterized neotectonic faults mimic the orientation of the respective modeled OOFs faults, we calculated the angular misfit following Aron et al. (2013), where a misfit $<22.5^\circ$ is accepted to consider the mapped faults as the OOFs conveniently oriented to be reactivated. Our models were performed considering an isotropic and elastic half-space with an effective coefficient of friction of 0.4, a Poisson’s ratio of 0.25 and, a Young’s modulus of $E = 80$ GPa, which have been adopted for previous ΔCFS analyses along the Chilean Andes (Bonali et al., 2013; Cortés-Aranda et al., 2015; Lupi and Miller, 2014). One of the limitations of our approach is that the postseismic viscoelastic relaxation of the upper plate was not modeled; however, the effects of this process are discussed in Section 5.2.

4. Results

4.1. Field data

4.1.1. Maihue area

Three sites with evidence of neotectonic deformation have been found at the southern border of the Maihue Lake and nearby the Mirador volcano (MiV; Fig. 2); these have been named, from north to south, MA1, MA2, and MA3 (Fig. 2a).

Site MA1 (Fig. 2a) consists of two outcrops at the southern border of the Maihue Lake: MA1a and MA1b (inset Fig. 2a and b). At the outcrop MA1a (Fig. 2), a 183/83 oriented fault juxtaposes Late Quaternary lacustrine varves with Holocene moraine deposits (Campos et al., 1998). This site was affected by a landslide following the 1960 Valdivia Earthquake (Fig. 2b). The fault at this outcrop has produced a deformation zone of 1.4 m width (Fig. 2c and d); within this zone, the varves are affected by sub-vertical fractures (yellow dashed lines in Fig. 2c) and the moraines show aligned clasts (Fig. 2d). By projecting this fault to the SE, a 30 m height scarp at the surface of the positive topography surrounding the lake can be observed (Fig. 2b). The outcrop MA1b is located 10 m westward MA1a (Fig. 2b); at this outcrop, a 025/84 fault drives 2 m of dextral offset of a channel-like feature in an abandoned lake terrace (Fig. 3a); this fault also produces a negative flower structure

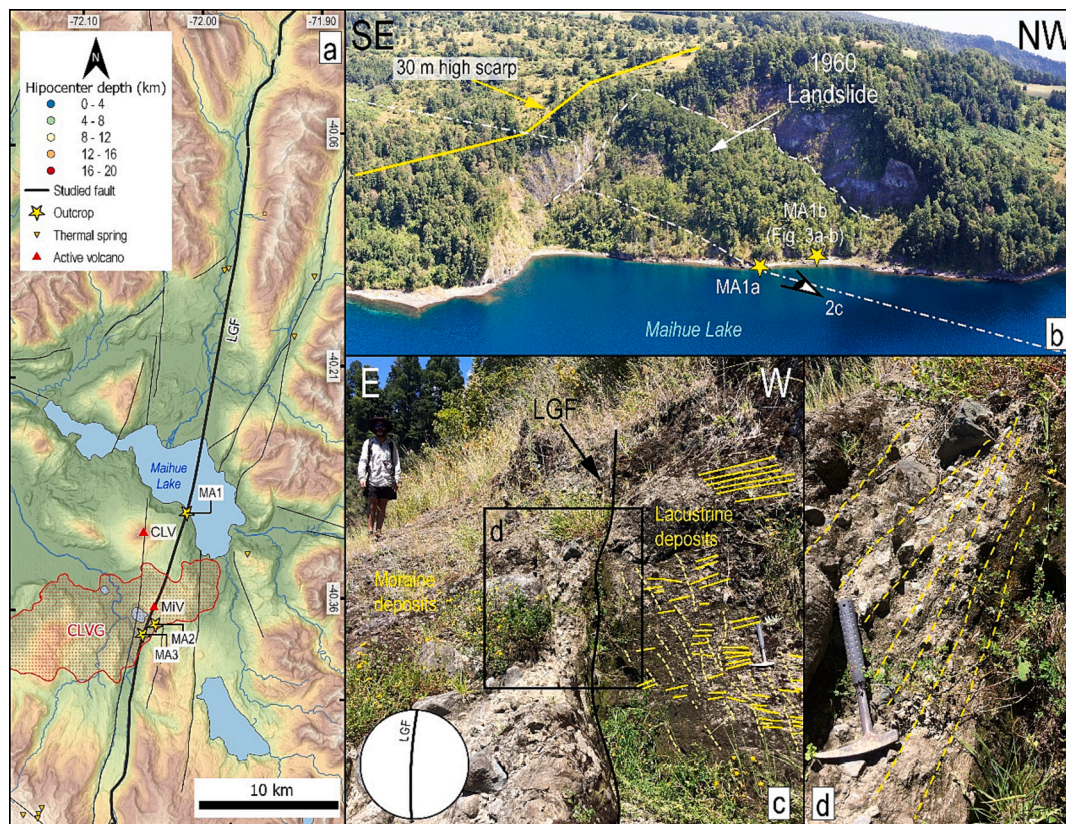


Fig. 2. Maihue area. a) Map of the Maihue area with crustal seismicity from IRIS, OVDAS, and Sielfeld et al. (2019). Major crustal faults from (FILLIN ""Maldonado et al., 2021). Yellow stars indicate the location of the MA1, MA2, and MA3 sites. LGF: Los Guindos Fault, CLV: Carrán-Los Venados Volcano; MiV: Mirador Volcano; CLVG: Carrán-Los Venados Volcanic Group (Bucchi et al., 2015). b) Southern border of the Maihue Lake. Dash-dotted white line indicates the LGF trace following the orientation measured at the MA1a outcrop. The white dashed line encloses the 1960 landslide. c) MA1a outcrop: The LGF puts in contact Holocene moraine deposits with Late Quaternary lacustrine varves. The person is 1.8 m tall. d) detail view of outcrop in C showing aligned clasts on the moraine along the fault damage zone. (For interpretation of the references to colour in this figure legend, the reader is referred to the web version of this article.)

in varve deposits internally limiting this terrace (inset Fig. 3a and b).

At the southern flank of the Mirador Volcano (MiV in Fig. 2a), we have found evidence of deformation in two sites (MA2 and MA3 in Fig. 2a); both expose Holocene pyroclastic deposits related to the Carrán-Los Venados Volcanic Group (CLVG; Bucchi et al., 2015). At site MA2 (Fig. 2a), a 032/78 oriented normal fault deforms laminated pyroclastic beds (Fig. 3e). At the base of the outcrop, layer deposits are offset 0.25 m along this fault; upwards, the same fault produces offsets of 0.1 m in these layer deposits. At site MA3 (Fig. 2a), a 315/60 oriented reverse fault has produced an offset of ca. 0.3 m in layers of the exposed pyroclastic deposits (Fig. 3f).

4.1.2. Las Pampas area

At the periphery of the Las Pampas Lake, ca. 15 km northwards the Liquiñe village (Fig. 4a), a bedrock channel draining from the lake towards the Liquiñe River exhibits a sharp dextral deflection (Fig. 4b). At the southern channel bend, a 2.5 m thick heavily weathered pyroclastic layer (Fig. 4g) was identified; this layer may be correlated with the Neltume pumice, an orange-pumice horizon with inferred ages of 12.4–10.3 ka (Rawson et al., 2015), the only pyroclastic deposit that has been recognized in the area (isopach contour in Fig. 4a). A well-developed soil horizon is located atop of this pumice (Fig. 4g). At this site, a fault-oriented 187/83 developed in tonalitic rocks of Mesozoic age (Lara et al., 2004), with sub-horizontal slickensides (Fig. 4f), is spatially consistent with the channel deflection; ~65 m upstream the deflection zone, a ca. 7 m high knickpoint occurs (Fig. 4d). By means of a high-resolution DSM, derived from photogrammetry, and using the present-day river channel as a marker of displacement, we estimate a Holocene cumulative offset of $162.8 \pm 4.2/-2.4$ m (Fig. 4e and f).

4.1.3. Palguín area

The Palguín Area is located at 39.43°S, at the periphery of the Palguín River (Fig. 5). There, a roadcut exhibits a sequence of deformed pyroclastic layers whose age ranges between 14 and 0.05 ka (Fig. 6a; Moreno Roa and Lara, 2008). The exposed section consists, from bottom to top, of an orange heavily weathered pumice horizon (SE1 in Fig. 6b) overlaid by a ca. 1.5 m thick laminated darkish and whitish sequence of pyroclastic deposits (SE2 in Fig. 6b). This latter level (SE2) is covered by a set of pumice layers interbedded with well-developed soil horizons (SE3 in Fig. 6b). The modern soil horizon develops atop of the section (SH in Fig. 6b). Charcoal samples from the SE3 unit (PA1–2 in Fig. 6b) and a pumice sample from the SE1 unit (PA3 in Fig. 6b) were collected to constrain the timing of deformation. The charcoal samples yield calibrated ages between ca. 8.8 and 8.4 ka BP (Figs. 6b, S1 and S2). In turn, the pumice analysis suggests that the PA3 sample can be correlated with the Neltume Pumice, dated in 12.4 to 10.3 ky by (Figs. 6b and S3 and Table S1; Rawson et al., 2015). At this outcrop, deformation concentrates at its southwestern part where south-dipping NE-striking faults accommodate reverse slip defining a fault zone of ca. 1.5 m width (Fig. 6b–d); the main fault has displaced 0.5 m the Neltume pumice layer (thick yellow line in Fig. 6c). Subparallel secondary faults accommodate minor reverse slip at the southwestern end of the outcrop (Fig. 6d). At the same outcrop, 5 m to the NNE of the main fault zone, folded layers were identified (Fig. 6e). The projection of the fault observed at this site towards the Palguín River is consistent with a notorious ca. 15 m high knickpoint (Fig. 6f). The GPR profile undertaken at this site (Fig. 6g) allowed observing the beds of the pyroclastic sequence at depth. This profile shows that the layers dip decreases towards the NNE (Fig. 6h and i). In addition, lateral discontinuities of the pyroclastic beds are

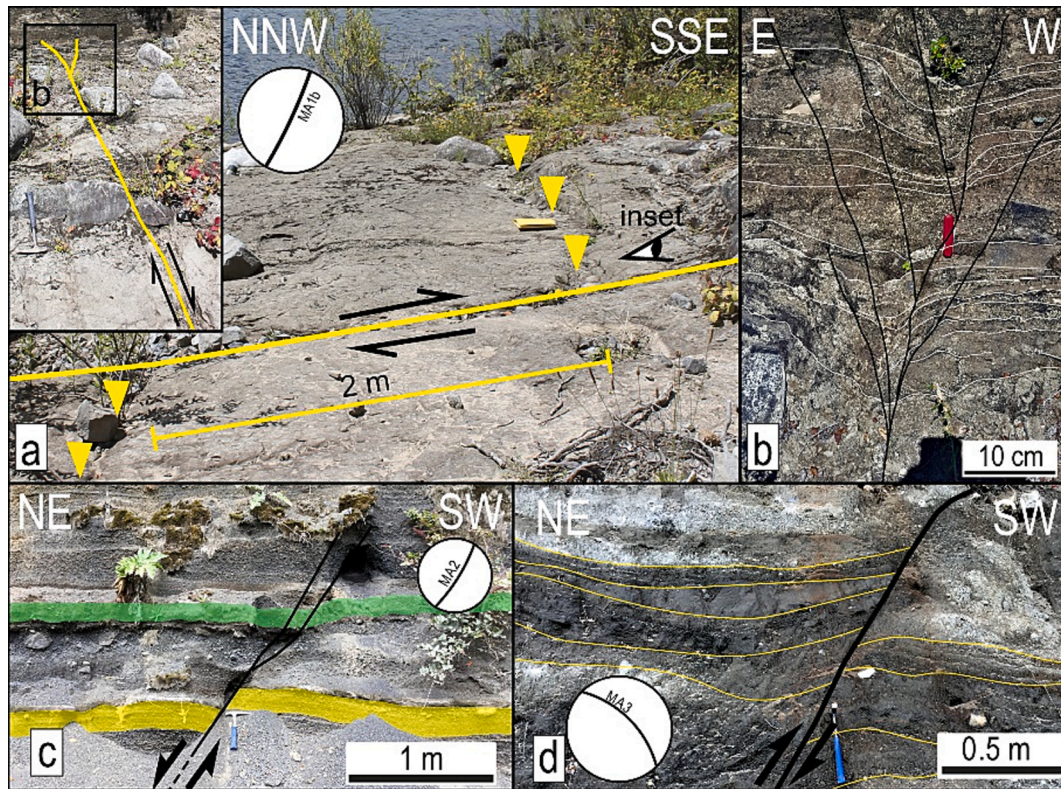


Fig. 3. Maihue area. a) Site MA1b: Stream-like feature dextrally displaced by the LGF trace. Inset shows the projection of this trace to the wall presented in b. b) Negative flower-structure developed on lacustrine deposits conducting centimetric scale deformation. c) Outcrop MA2: Holocene pyroclastic deposits affected by a NE-oriented normal fault. d) Outcrop MA3: The same pyroclastic deposits from C affected by a NW-striking reverse fault.

observed in the GPR profile (Fig. 6i), directly beneath the faults visible at the outcrop of Fig. 6b.

4.1.4. Caburgua area

The Caburgua Lake is an intra montane lake of the Villarica lake Basin. In this area, we have identified three sites (CA1, CA2, and CA3 inset in Fig. 7a) exhibiting deformed Late Holocene pyroclastic deposits ranging in age between 14 and 0.05 ka (Moreno Roa and Lara, 2008). All the sites are located at the southeastern border of Caburgua Lake (Fig. 7a). Formerly, Hernandez-Moreno et al. (2014) reported evidence for normal and reverse faults affecting these deposits near the Caburgua Area.

In site CA1 (inset Fig. 7a), well-laminated pyroclastic deposits are deformed by an ESE-dipping normal fault (Fig. 7b). This fault cuts the entire sequence and has conducted displacements up to 8 cm along the fault plane, the layers exhibit drag folds towards the fault plane, supporting the inferred fault kinematics (inset in Fig. 7b). In site CA2 (Fig. 7c), well-laminated pyroclastic deposits are deformed by a set of NW-striking southwest dipping normal faults (123/35); these faults seem to converge at depth and led normal offsets ranging between 0.05 m and 0.5 m of well-identified markers (Fig. 7c). At site CA3 (Fig. 7a), a pyroclastic sequence is affected by a 019/33 oriented fault (Fig. 8a). The fault exhibits a minimum observed normal displacement of 4.2 m along the fault plane. Minor secondary faults splay from the main structure towards the hanging wall exhibiting both normal and reverse displacements (Fig. 8b–d).

4.1.5. Analysis of the reported evidence

The herein documented evidence indicates that the Late Quaternary kinematics of the intra-arc faults in the study area (39–40.5°S) is complex and variable along its trend.

Evidence from the Maihue Area (sites MA1a–b; Figs. 2 and 3) suggests dextral displacements along NNE-striking faults; for that area, the

Los Guindos Fault (LGF; Figs. 2 and 3), a ca. 65 km long dextral fault has been formerly mapped (Astudillo-Sotomayor et al., 2021; Guzmán-Marín et al., 2015). We thus consider that the herein reported evidence has been produced by the LGF during the Late Quaternary. Despite this area was affected by a landslide following the 1960 Valdivia Earthquake, it must be noted that deformed deposits are well-consolidated, thus unlikely perturbed by this mass-wasting event. Moreover, the scarp related to this landslide is oriented N45E, notably differing from the NNE orientation of the herein reported faults. In addition, the evidence at the outcrop scale is coherent, in terms of its orientation, with the regional strike of the LGF. These observations confirm that the evidence found in sites MA1a–d has been caused by tectonic faulting. Sites MA2 y MA3 indicate, respectively, normal faulting on a NE-striking fault and reverse faulting on an EW-striking fault. These faults do not seem to correspond to any former mapped structure or lineament in the periphery, so we interpret them as secondary structures of the LGF.

At the Las Pampas Area, the fault driving the dextral offset of the studied bedrock channel corresponds, according to its orientation and geographical position, to the Liquiñe Fault (LiF in Fig. 4). This fault was defined by Astudillo-Sotomayor et al. (2021) 15 km southwards; the Liquiñe Fault is a 185/85 oriented fault that has promoted a dextral inflection – by ca. 170 m – on the Liquiñe River bedrock channel. From the age of deformed fluvial and pyroclastic deposits, a slip rate of 18.8 m/ka has been proposed for the last 9 ky (Astudillo-Sotomayor et al., 2021). Given the similarity between these two offset estimations, it is likely that the deformation observed at Las Pampas is contemporary with the Liquiñe Site from Astudillo-Sotomayor et al. (2021).

In the Palguín Area, the neotectonic evidence suggests Holocene reverse slip along a SE-dipping structure. Despite no faults with this orientation and kinematics have been formerly mapped in the area, a NE-striking lineament defining the SW border of the Villarica Volcano (Sánchez et al., 2013) is coherent with the herein reported evidence, the occurrence of thermal springs, and shallow seismic events reported by

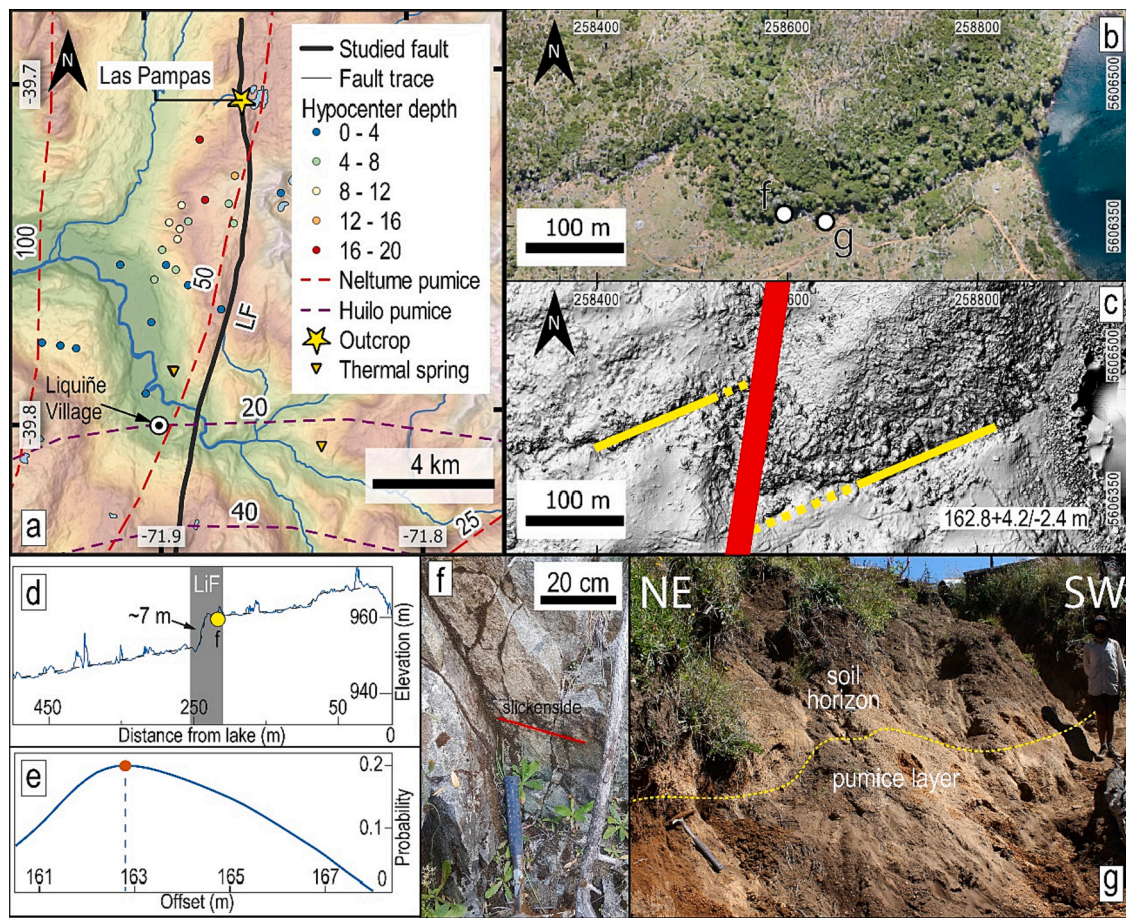


Fig. 4. Las Pampas area. a) Map of the Las Pampas area. Isopach contours for pumice deposits from (FILLIN ^{""}Rawson et al., 2015). Black thick line corresponds to the Liquiñe Fault from (FILLIN ^{""}Astudillo-Sotomayor et al., 2021). Scattered shallow crustal seismicity from IRIS database, and Sielfeld et al. (2019). b) Aerial view of Las Pampas Outcrop. Location of sites for f and g are shown with white circles. c) Hillshade showing the location of the offset markers (dashed/continued yellow lines) and fault trace (thick red line). d) Longitudinal profile of the stream; note the ca. 7 m high knick point along the profile. e) Offset pdf for the river canyon; orange circle marks the mean value. f) Outcrop of a fault plane developed over tonalitic rocks with sub-horizontal slickensides (red line). g) Outcrop at the southern border of the stream. (For interpretation of the references to colour in this figure legend, the reader is referred to the web version of this article.)

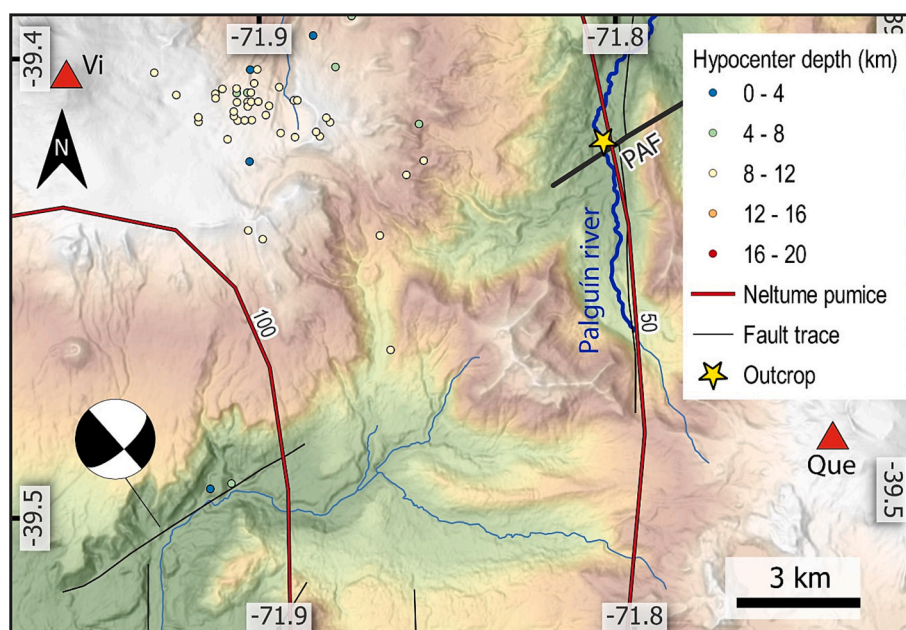


Fig. 5. Map of the Palguín area. Red segment line is the isopach contour (thickness in cm) for the Neltume Pumice from Rawson et al. (2015). Crustal seismicity from IRIS database and (FILLIN ^{""}Sielfeld et al., 2019). Focal mechanism from Sielfeld et al. (2019). The thick blue line represents profile trace in 6 f. PAF: Palguín Fault. Vi: Villarrica volcano. Que.: Quetupillán volcano. (For interpretation of the references to colour in this figure legend, the reader is referred to the web version of this article.)

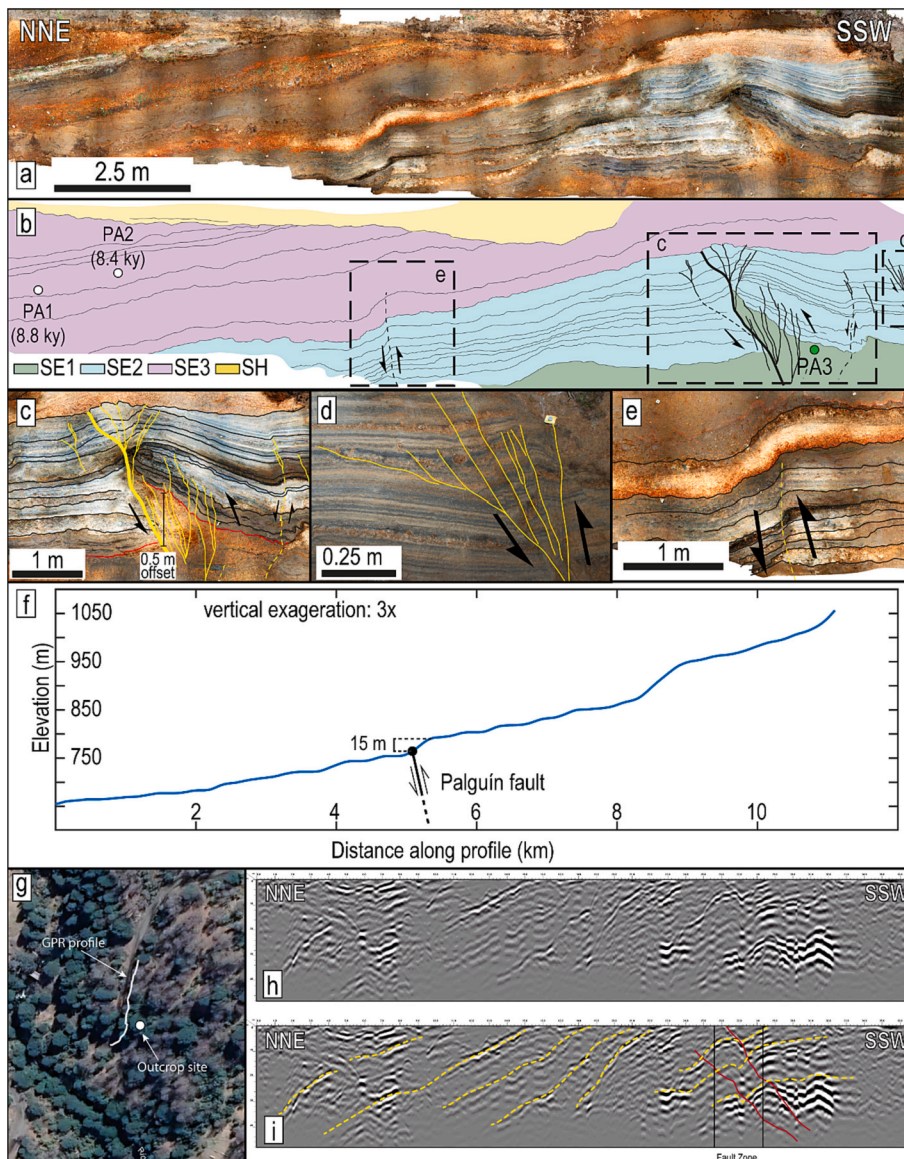


Fig. 6. Palguín site. a) Holocene pyroclastic sequence deformed by the Palguín Fault. Note the change in the dip of the layers and the deformed lower portion of the sequence. b) Diagram of the outcrop situation depicting mapped fault traces and sampling points (white for charcoal and green for pumice). SE1, SE2, SE3 and SH are referred in the text. c) Main fault zone at the outcrop; thick yellow line corresponds the major fault, and thin lines depict secondary faults playing from the major one. Red lines indicate the top of the Neltume pumice layer. d) Minor secondary faults with reverse kinematics. e) Monoclinical fold of the pyroclastic sequence. f) Longitudinal river profile of a segment of the Palguín river (see Fig. 5 for profile trace), the location of the Palguín Fault is spatially consistent with a knickpoint of ca. 15 m high. g) Google Earth view of the GPR profile trace (white line), the white circle depicts the location of the outcrop showed in a. h) GPR profile processed data. i) Interpretation of the GPR profile data. Yellow dashed-lines correspond to the interpreted layers of the pyroclastic sequence, and the red solid-lines correspond to the interpreted faults. (For interpretation of the references to colour in this figure legend, the reader is referred to the web version of this article.)

Sielfeld et al. (2019) (focal mechanism in Fig. 5). With these data, we herein define the Palguín Fault (PaF), a 25 km long fault producing reverse slip during the Holocene. The kinematics and geometry of the PaF are inconsistent with the overall orientation of the volcanic arc of the Patagonian Andes. Nevertheless, at the latitude of the Palguín Site, the LOFS is crossed by the Mocha-Villarrica Fault Zone (MVZF in Fig. 1b), a crustal-scale sinistral transpressive fault with NW orientation (Rosenau et al., 2006). The deformation induced by the MVZF could alter the geometric and kinematic pattern of the volcanic arc, thus allowing the occurrence of structures such as the PaF.

The Caburgua Area exhibits evidence for normal faulting both on a NNE-striking fault and on a NW-striking fault. The first one, because of its orientation and geographical position, would correspond to the 21 km length NS-striking fault mapped in the area by Moreno Roa and Lara (2008); according to Sánchez et al. (2013), Holocene volcanic cones align with this fault (Fig. 7). Since no names have been formerly proposed for this fault, we refer to this structure as Northern Caburgua Fault (NCF in Fig. 7a). With our data, we demonstrate that this fault has experienced normal slip during the Holocene. In turn, deformation visible at the outcrop in site CA2 can be related to a 7 km length lineament of thermal springs and microseismicity (Sielfeld et al., 2019) eastwards the Caburgua lake. Based on these antecedents, we propose

the occurrence of the Eastern Caburgua Fault (ECF in Fig. 7a); its strike is parallel to another seismic lineament documented 7.5 km northwards by Sielfeld et al. (2019) (Fig. 7a). Our field evidence allows proposing that this fault has driven normal slip during the Holocene.

4.2. Coulomb failure stress change (ΔCFS)

In the former section, based on field evidence, we have proposed the occurrence of 5 active faults of different orientations and kinematics at the northern LOFS. Herein, we present the ΔCFS results – induced by the 1960 Valdivia Earthquake and the former interseismic period – onto dextral, reverse, and normal Optimally Oriented Faults (OOFs) in the study area; based on this, we then discuss the possible influence of the modeled stages of the subduction cycle in triggering the herein defined neotectonic faults. Table 1 presents a summary of the ΔCFS values induced along the studied faults and the angular misfit between them and the modeled OOFs.

4.2.1. ΔCFS induced by the Mw 9.5 Valdivia 1960 earthquake

For dextral OOFs, the ΔCFS induced by the 1960 Valdivia earthquake varies between 2.42 and 11.22 bar; this ΔCFS field exhibits a smooth W-E decreasing gradient (Fig. 9a). Dextral OOFs (black lines in Fig. 9a) are

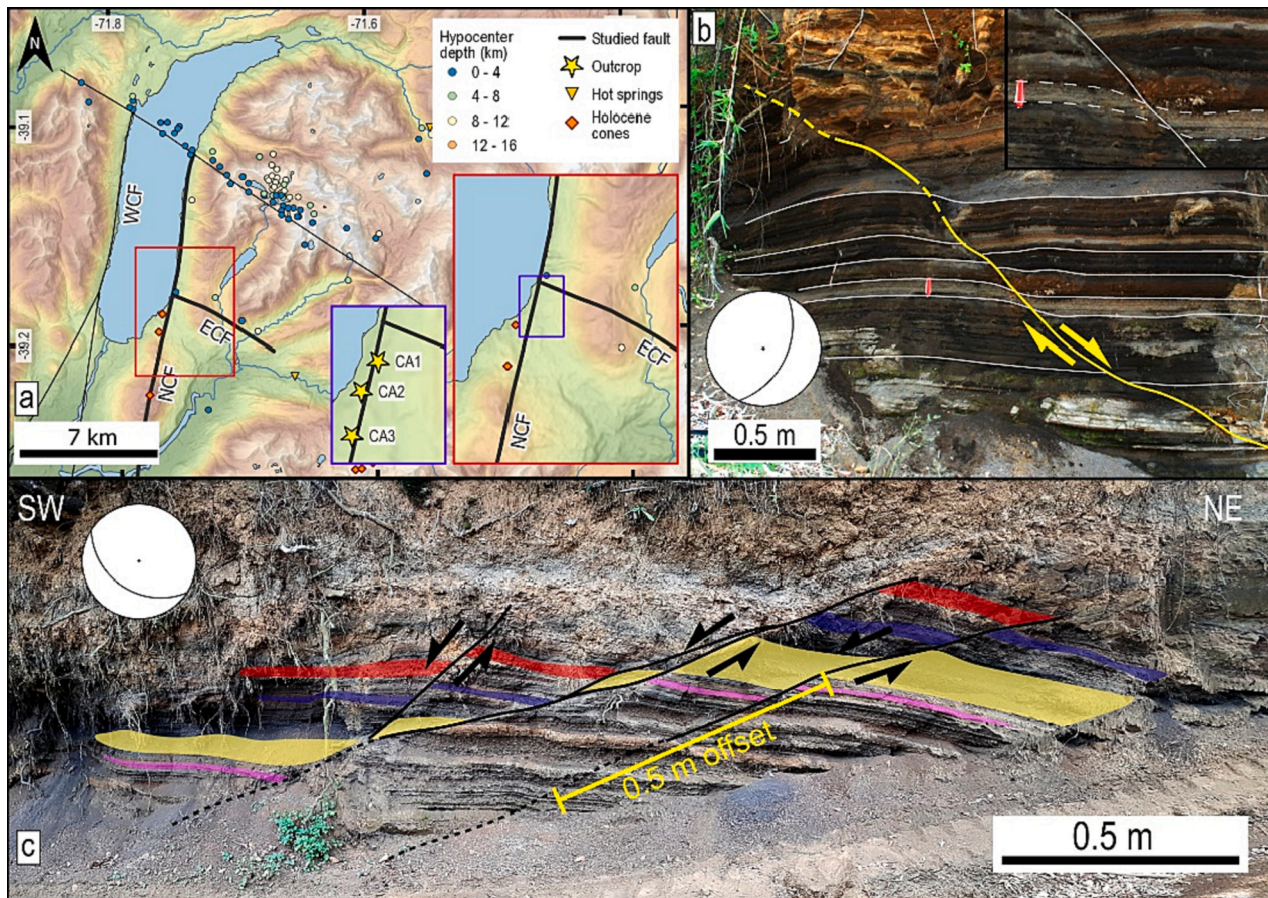


Fig. 7. Caburgua area. A) Map of Caburgua area. Fault traces from Maldonado et al. (2021). Seismicity from Sielfeld et al. (2019). Inset shows the location of the three different outcrops identified in this area. ECF: Eastern Caburgua Fault. B) Site CA1 exposing a E-ESE dipping fault plane affecting postglacial pyroclastic deposits. Centimeter scale offsets along the sequence attest for normal displacements along the fault. C) Site CA2 exposing a SSW-dipping fault zone affecting deposits of the same pyroclastic sequence than in CA1. Displaced layers suggest normal kinematics for these faults.

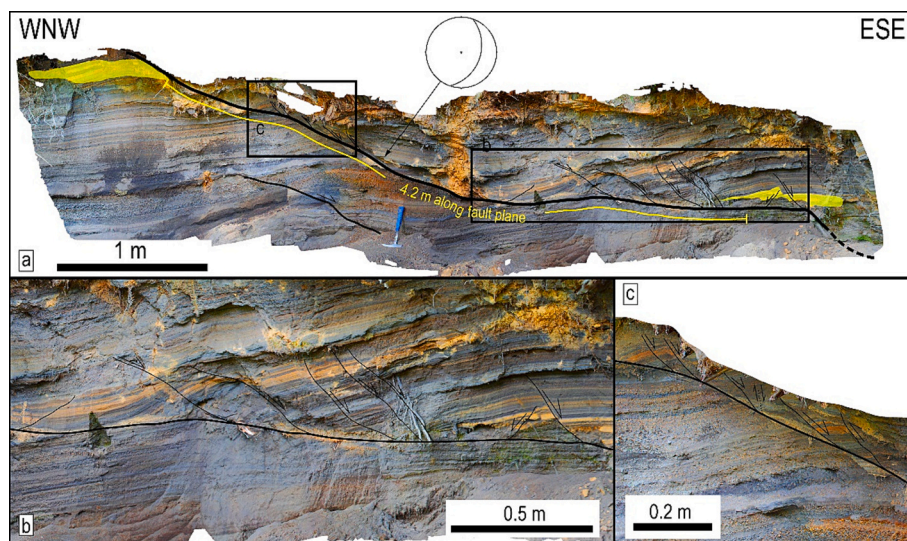


Fig. 8. Site CA3. A) Holocene pyroclastic sequence deformed by an ESE dipping normal fault. The major fault has conducted displacements of ca. 4.2 m along the fault plane; minor secondary normal, and reverse faults splay from the major trace and exhibit centimeter-scale offsets. B) Detail of the eastern lower portion of the fault zone with several splay faults developed on the hanging wall. C) Detail of the upper western upper section of the outcrop with more secondary faults developed on the hanging wall of the fault.

dominantly SSE striking (mean value 163° ; see rose diagram in Fig. 9a). The modeled dextral OOFs show an intermediate misfit ($<22^\circ$; see misfit scale in Fig. 9d and Table 1) with respect to the strike of the LGF, the LiF, and the NCF (Fig. 9d). In turn, the modeled dextral OOFs present high misfit values ($>48^\circ$; see misfit scale in Fig. 9d and Table 1) with respect

to the orientation of the PaF and the ECF (Fig. 10d). All the mapped faults (LGF, LiF, PaF, NCF and ECF) lie in zones with positive ΔCFS values varying between 3.73 and 7.32 bar (Table 1 and Fig. 9a).

The ΔCFS values for OOFs of reverse kinematics range between -1.74 and -0.44 bar, showing a smooth increasing trend (Fig. 9b).

Table 1

Coseismic and interseismic Δ CFS values at each studied fault, and angular misfit between them and the modeled OOFs. Angular misfit classes: low (misfit $<20^\circ$); moderate (mod; $20^\circ < \text{misfit} < 40^\circ$); and high: misfit $>40^\circ$. LGF: Los Guindos Fault; LiF: Liquiñe Fault; PaF: Palguín Fault; NCF: Northern Caburgua Fault; ECF: Eastern Caburgua Fault.

Slip	Fault	Coseismic CFS			Interseismic CFS		
		Misfit	Δ CFS (bar)		Misfit (deg)	Δ CFS (bar)	
			min	max		min	max
Dextral	LGF	21–22	6.76	7.32	16	1.29	2.15
	LiF	20	5.83	6.42	14–15	1.45	2.06
	PaF	65	4.95	5.42	60	1.73	2.71
	NCF	22	3.73	4.77	17	1.95	3
	ECF	48	3.88	4.12	53	1.35	2.02
Reverse	LGF	77	−0.9	−0.67	71	2.85	3.30
	LiF	76	−0.66	−0.64	70	3.18	3.44
	PaF	59	−0.72	−0.76	64	3.48	3.71
	NCF	78	−0.89	−0.79	73	3.62	3.85
	ECF	8	−0.84	−0.80	3	3.46	3.69
Normal	LGF	12	7.38	8.17	18	−1.66	−0.89
	LiF	14	6.49	7.03	20	−1.65	−1.22
	PaF	31	5.68	6.17	25–26	−1.59	−1.07
	NCF	11	4.67	5.65	17	−1.72	−0.99
	ECF	81	4.70	5.0	87	−2.16	−1.61

Reverse OOFs (black lines in Fig. 9b) are dominantly SSE striking (mean value 107° , see rose diagram in Fig. 9b). These modeled reverse faults show a high misfit (48° – 78° ; see misfit scale in Fig. 9e and Table 1) with respect to the orientation of the LGF, the LiF, the PaF, and the NCF (Fig. 9e). Reverse OOFs exhibit a low misfit (8° ; see misfit scale in Fig. 9e and Table 1) with respect to the strike of the ECF (Fig. 9e). All the mapped faults lie in zones with negative Δ CFS values, ranging between -0.90 and -0.64 bar (Table 1 and Fig. 9b).

In the case of normal OOFs, Δ CFS range between 3.14 and 12.14 bar, with the highest values concentrated at the NW domain of the area (Fig. 9c). The modeled normal OOFs (black lines in Fig. 9c) are mostly NNE-oriented (mean value 17° , see rose diagram in Fig. 9c). The modeled normal OOFs have low misfit (9° – 12° ; see misfit scale in Fig. 9f and Table 1) with respect to the strike of the LGF, the LiF, and the NCF (Fig. 9f). In turn, normal OOFs present, respectively, intermediate (33° ; see misfit scale in Fig. 9f and Table 1) and high (79° ; see misfit scale in Fig. 9f and Table 1) misfit with respect to the orientation of the PaF and the ECF (Fig. 9f). The mapped faults lie in zones where the Δ CFS is positive and ranging between 4.70 and 8.17 bar (Table 1 and Fig. 9c).

4.2.2. Δ CFS for the interseismic scenario

The Δ CFS induced for dextral OOFs is in the range between -2.34 and 12.51 bar (Fig. 10a). Dextral OOFs show a marked SSE orientation within the entire study area (mean 168° , see rose diagram in Fig. 10a) and the Δ CFS values show a northwestward increasing trend (Fig. 10a). Dextral OOFs have a low misfit (14° – 17° ; see misfit scale in Fig. 10d and Table 1) with respect to the orientation of the LGF, the LiF and the NCF (Fig. 10d). Modeled dextral OOFs exhibit high misfit (53° – 60° ; see misfit scale in Fig. 10d and Table 1) relative to the strike of the PaF and the ECF.

(Fig. 10d). The mapped faults lie in areas where the Δ CFS is positive, ranging between 1.29 and 2.71 bar (Table 1 and Fig. 10a).

The obtained Δ CFS for reverse OOFs is within the range between 1.32 and 6.70 bar, defining a WNW increasing trend (Fig. 10b). The modeled OOFs show a marked SE orientation (median 112° ; see rose diagram in Fig. 10b). These reverse OOFs have a high misfit (64° to 73° ; see misfit scale in Fig. 10e and Table 1) with respect to the strike of the LGF, the LiF, the NCF, and the PaF (Fig. 10e). In turn, reverse OOFs exhibit a low misfit (3° ; see misfit scale in Fig. 10e and Table 1) relative to the orientation of the ECF (Fig. 10e). All the studied faults are in zones with Δ CFS values ranging from 2.85 to 3.30 bar (Table 1 and Fig. 10b).

For normal OOFs, the Δ CFS values are between -4.91 and 5.57 bar

(Fig. 10c). These modeled faults are dominantly ENE oriented (mean 22° , see rose diagram in Fig. 10c). Modeled normal OOFs have a low misfit ($<18^\circ$, see misfit scale in Fig. 10f and Table 1) with respect to the strike of the LGF and the NCF (Fig. 10f). In turn, normal OOFs present intermediate misfit (20° – 26° ; see misfit scale in Fig. 10f and Table 1) with respect to the orientation of the LiF and the PaF (Fig. 10f); a high misfit (87° ; see misfit scale in Fig. 10f and Table 1) was determined between the orientations of the normal OOFs and the mapped ECF (Fig. 10f). The Δ CFS values for all the mapped faults are in the range -2.16 to -0.89 bar (Table 1 and Fig. 10f).

5. Discussion

5.1. On the nature of the reported evidence

In this paper, we have interpreted that the reported deformation is related to tectonic processes (e.g., faulting or folding). Nevertheless, at least for those cases where the evidence corresponds to offset pyroclastic layers (e.g., Palguín and Caburgua areas), one may argue that deformation is due to non-tectonic factors like syn-eruptive and/or gravitational processes; these processes can involve faulting of different kinematics. Syn-eruptive deformation can be driven by processes like shearing between flows, gravity, ballistic impacts, etc.; the developed structures can be similar to those originated by tectonic faulting and/or folding in fold and thrust belts (Douillet et al., 2015). Evidence of this kind has been documented, for instance, in the Ubehebe craters in Death Valley California (Douillet et al., 2015; Valentine et al., 2021), and in the Laach Lake, in Germany (Douillet et al., 2015). Given its origin, syn-eruptive deformational processes tend to affect only a discrete portion of the sedimentary sequence. On the other side, normal faulting of non-tectonic origin could be related to gravitational processes like grav-iquakes or mega-landslides (Douillet et al., 2015). Despite its non-tectonic origin, when the fault plane penetrates deep in the crust may produce Mw > 5.5 earthquakes, like the Mw 7.2 earthquake in 1975 along the Kalapana Fault, on the Island of Hawaii, or the faults located at the eastern flank of Mount Etna, Sicily (McCalpin, 2009). This kind of structures occur at the flanks of very large volcanoes and exhibits a curve profile in plan view (McCalpin, 2009). In our case, it is very unlikely that the deformation observed at the Palguín area was generated by gravitational processes, given the reverse kinematics of the PaF. A syn-eruptive origin it is also unlikely, because the PaF cuts pyroclastic layers of different ages, thus suggesting that it formed long time after the causative eruptions. These conditions, besides the fact that even deeper portions of the pyroclastic sequence are deformed by this fault (Fig. 6i and j), led us to consider that the evidence at the Palguín Site is primarily led by tectonic forces. For the faults observed at the Caburgua area, we consider unlikely a syn-eruptive origin, given the distance between the outcrops and the major volcanoes in the area (e.g., Villarrica, Quetrupepillán volcanoes). On the other hand, we cannot completely rule out a gravitational origin for the deformation within this area, considering the kinematics of the causative faults (Figs. 7 and 8). Nevertheless, the mapped trace of the related structures on the CHAF database (Maldonado et al., 2021) are very straight, suggesting that the origin of these structures is not related to gravitational processes. These facts led us to infer that tectonic faulting is the first order process behind the evidence at the Caburgua Site. For both areas, Palguín and Caburgua, the interpretation of tectonic faulting as the main factor producing the reported deformation is supported by the clear spatial link between the faults observed at the outcrops and regional faults/lineaments, some of these related to instrumental seismicity (e.g., Sielfeld et al., 2019).

The reported neotectonic deformation is accommodated by N-S oriented normal faults (NCF; Figs. 7 and 8), NNE dextral faults (LGF and LiF; Figs. 2 and 4), NW normal faults (ECF; Fig. 7), and the NE reverse Palguín Fault (PaF; Fig. 6). Despite the great variability in kinematics and fault orientation, all the structures seem to have been active during the same time span (Late Quaternary) and are coherent with the

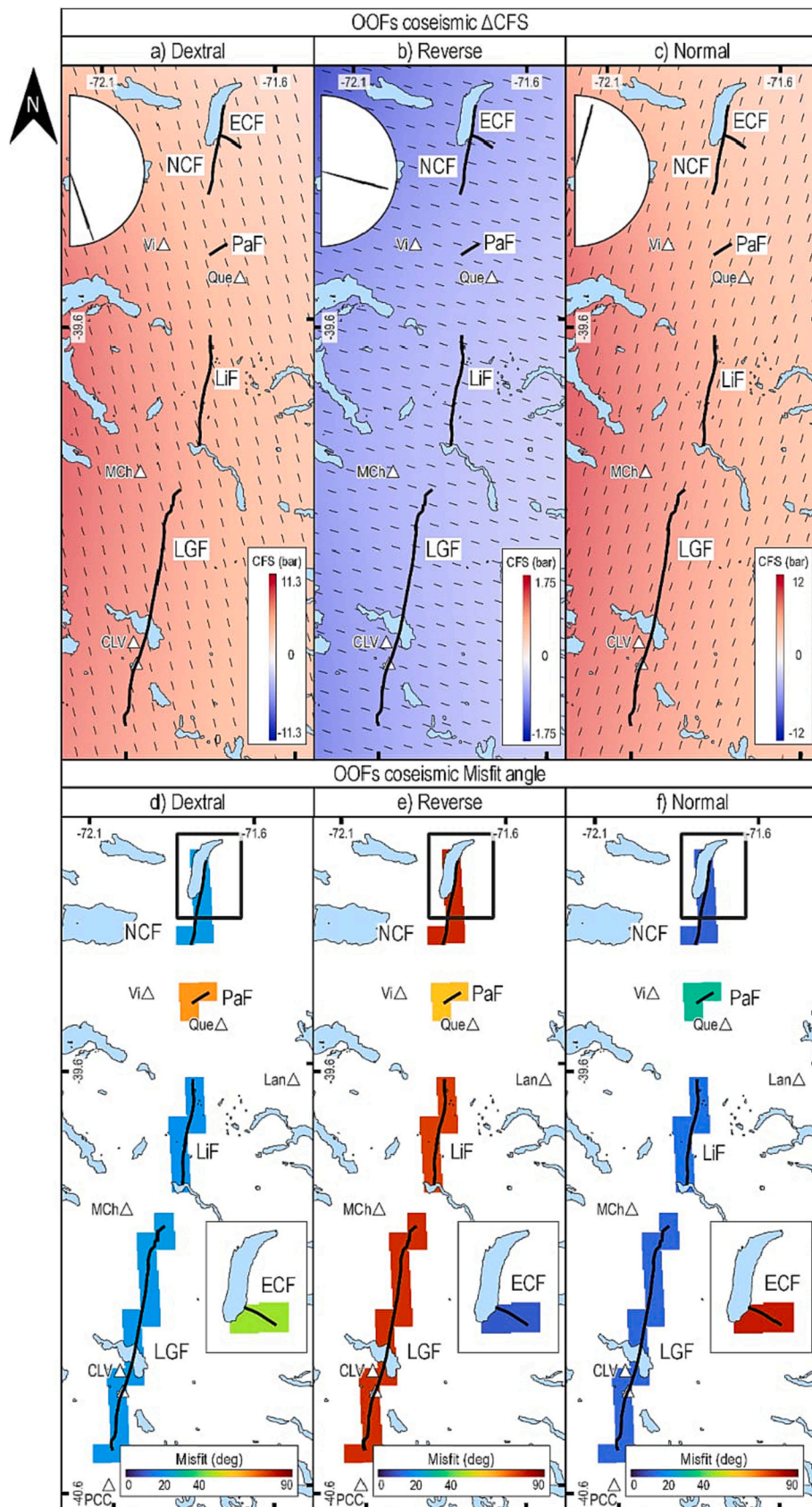


Fig. 9. ΔCFS induced by the coseismic slip of the Valdivia 1960 earthquake. Thick black lines depict the trace of our studied faults, thin black lines correspond to the strike of the OOFs at each grid cell. **NCF:** Northern Caburgua Fault, **ECF:** Eastern Caburgua Fault; **PaF:** Palguín Fault; **LiF:** Liquiñe Fault; **LGF:** Los Guindos Fault; **Vi:** Villarrica; **Que:** Quetrupillán; **Lan:** Lanín; **MCh:** Mocho-Choshuenco; **CLV:** Carrán-Los Venados; **MiV:** Mirador Volcano; **PCC:** Pulehue-Cordón Caulle. A to C) ΔCFS induced by the coseismic slip of the Valdivia earthquake for dextral, reverse, and normal OOFs, respectively; rose diagrams show the strike of the OOFs in each case. D to F) Misfit angle between OOFs and the studied faults. The inset map depicts the misfit angle for the ECF. (For interpretation of the references to colour in this figure legend, the reader is referred to the web version of this article.)

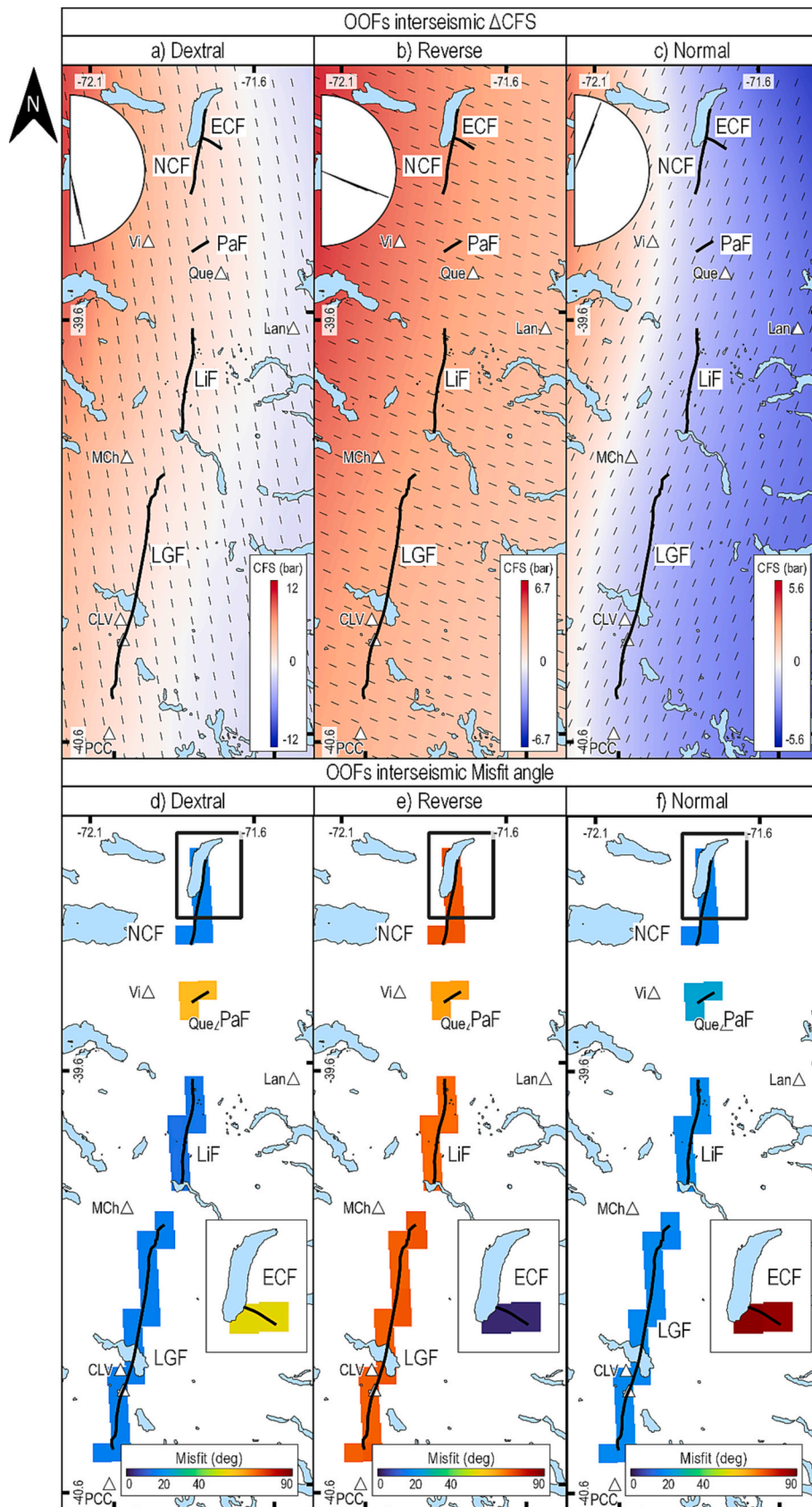


Fig. 10. Δ CFS induced by the interseismic scenario. In each case, thick black lines depict the trace of our studied faults, while thin black lines correspond to the strike of the OOFs at each grid cell. **NCF:** Northern Caburgua Fault; **ECF:** Eastern Caburgua Fault; **PaF:** Palguín Fault; **LiF:** Liqueñe Fault; **LGF:** Los Guindos Fault; **Vi:** Villarrica; **Que:** Quetrupeñán; **Lan:** Lanín; **MCh:** Mocho-Choshuenco; **CLV:** Carrán-Los Venados; **MiV:** Mirador Volcano; **PCC:** Pulehue-Cordón Caulle. A to C) Δ CFS induced by the coseismic slip of the Valdivia earthquake for dextral, reverse, and normal OOFs, respectively; rose diagrams show the strike of the OOFs. D to F) Misfit angle between OOFs and the studied faults. The inset map depicts the misfit angle for the ECF. (For interpretation of the references to colour in this figure legend, the reader is referred to the web version of this article.)

structural grain that characterizes this part of the intra-arc (Cembrano et al., 1996; Lavenue and Cembrano, 1999; Peña et al., 2021; Pérez-Flores et al., 2016; Rosenau et al., 2006). North of our study area, several works have reported evidence of Late Quaternary deformation related to dextral transpression along the northern end of the LOFS (Melnick et al., 2006a, Melnick et al., 2006b), and along the Antñir-Copahue Fault System, at the eastern slope of the Andes (Colavitto et al., 2020; Folguera et al., 2004; Jagoe et al., 2021). This evidence suggests that, north of 40.5°S, most of the LOFS segments have been active during the Late Quaternary.

The main challenge when dealing with neotectonic evidence is unraveling its origin in terms of the mechanics – aseismic and/or seismic – of the causative processes. Up to date, no data attesting for an aseismic behavior of the LOFS, and related faults have been acquired; devoted GPS experiments should be carried out to shed light on this topic. On the other hand, the available data suggest that these faults can produce moderate to large earthquakes (Lange et al., 2008; Pérez-Estay et al., 2020; Sielfeld et al., 2019). The clearest evidence in this sense is given by the occurrence of the Aysén Seismic Crisis in 2007 (Legrand et al., 2011). Russo et al. (2011), based on the study of the triggered seismic activity during this crisis, reinforces the LOFS seismogenic behavior. They base this suggestion on the idea that the LOFS was close to failure by at least 4 months during the crisis, and that the accumulated stress was released by five Mw 5.2–6.2 earthquakes instead of a cascading rupture ending with a larger seismic event. Considering this evidence, it may be reasonable to attribute the herein reported field evidence to past earthquakes. Under this assumption, an interesting point to discuss is the magnitude of the causative paleoearthquakes. For the study area, a convex seismogenic bottom layer is defined by Sielfeld et al. (2019); beneath the volcanic chain of the intra-arc, this layer is situated at ca. 12 km depth. We consider this depth as the seismogenic extent for the studied faults; this, besides the mapped length in each case, allowed approaching the rupture area for the studied faults (Table 2 and Fig. 11a). The rupture area was then considered to estimate the Mw of the earthquakes that can be produced by each fault following the empirical relations of Thingbaijam et al. (2017). The obtained Mw range between 5.5 and 6.8 for the different faults (Fig. 11a and Table 2). Based on the same relations, we then estimated the coseismic average slip associated with each earthquake (Table 2 and Fig. 11b). The obtained values range between 0.08 and 0.6 m; these values suggest that only the offset produced by the PaF in Holocene pyroclastic deposits (0.5 m; Fig. 6c) may be related to one single thrust event of Mw 6.3. For the remaining cases, the measured offsets would represent the cumulative effect of repeated paleoearthquakes.

Late Quaternary and Holocene slip rates for individual LOFS branches have been recently determined (De Pascale et al., 2021 and Astudillo-Sotomayor et al., 2021, respectively). These rates vary between 11 and 24 mm/y and have been estimated for first-order NNE-striking LOFS branches. If the Late Quaternary slip rates for the herein studied faults range into this interval, the recurrence for Mw 5.5 to 6.8 earthquakes would be on the order of 7 to 50 years. This figure is not in agreement with what the historical record for crustal seismicity along the LOFS and spatially related faults shows. Further, this is two orders of magnitude shorter than the 2 ky recurrence time suggested for

earthquakes along the LOFS from the stratigraphic analysis of a core drilled in the Aysén Fjord (Wils et al., 2018). This discrepancy insinuates that fault creep may have a preponderant role in explaining the herein reported deformation. Overall, this suggests that crustal intra-arc faults in Southern Chile may behave both as aseismic and seismic structures.

Even if aseismic slip on the herein studied faults – and other structures in the Southern Chile intra-arc – may be significant, we consider that their seismic capacity must not be neglected. In general, crustal faults remain quiet for long periods, from decades to thousands of years (Slemmons and dePolo, 1986), before producing an earthquake. Other faults, however, accommodate aseismic slip during long periods, but generate also microseismicity (e.g., Harris, 2017) and even moderate-to-large earthquakes (e.g., Oppenheimer et al., 2010). It is the case, for instance, of faults in California. There, the Parkfield segment of the San Andreas Fault system regularly produces M6 earthquakes (Bakun et al., 2005) but experiences also shallow creep (e.g., Johanson, 2006). Likewise, the Hayward Fault has been able to produce M6.8 earthquakes (Bakun, 1999) and also creeps regularly both at shallow and deep portions of the crust (e.g., Chaussard et al., 2015). This seismic/aseismic behavior has been also determined for trench-parallel strike slip faults in active volcanic arcs; it is the case, for example, of the Great Sumatran Fault (GSF) in Indonesia. At its northern end, the Aceh segment of this fault is characterized by producing shallow (<16 km) microseismicity ($M_L \leq 4$) and Mw > 6 earthquakes as those of 2013 and 2016 (Muksin et al., 2019). However, aseismic slip has been also determined for this fault segment up to 10 km depth (Ito et al., 2012; Tong et al., 2018). The mechanisms behind this dual behavior would be related to a complex depth-dependent layering of the crust, involving velocity strengthening (aseismic) and velocity-weakening (seismic) levels (Scholz, 1998). Based on this, (Harris, 2017) infers that even dominant creeping faults present dispersed locked zones, which would be able to produce earthquakes. Even though the herein presented data do not allow for accurately discussing the mechanics of the studied faults, we hypothesize that this structure may behave similarly to other strike-slip faults experiencing both creep and seismic behaviors. This reinforces the idea of considering the herein defined neotectonic faults – and in general the intra-arc faults in the area – for seismic hazard appraisals.

5.2. Megathrust earthquake cycle and intra-arc fault reactivation

According to our results, both the Valdivia 1960 Earthquake and the interseismic period promote favorable conditions to reactivate intra-arc faults in the study area. Two of the neotectonic faults herein defined – the dextral LGF and the dextral LiF (Figs. 9a and 10a) – were moved to failure (positive ΔCFS ; misfit <22.5°) by the two modeled scenarios (Fig. 9a and c; Table 1). One – the normal NCF – was exclusively favored coseismically (Fig. 9c and d; Table 1). In turn, two of the defined faults, the PaF and the ECF, are not favored (negative ΔCFS and/or misfit <22.5°) to slip neither in the coseismic nor in the interseismic model (Table 1; Figs. 9 and 10).

Former works have discussed the significance of a gradual (as represented by our interseismic scenario) versus a sudden (as represented by our coseismic scenario) stress augmentation along receiver faults to trigger seismicity (Dieterich, 1994; Toda and Stein, 2003). Due to a gradual stress increase, seismicity along the receiver faults tends to equal the background seismicity and is assumed constant (Toda and Stein, 2003). On the other hand, it has been proposed that when a sudden stress perturbation occurs, a ΔCFS increment may augment the seismicity rate along the receiver faults (Dieterich, 1994; Toda and Stein, 2003). Thus, it can be suggested that crustal fault reactivation is more likely to occur due to stress perturbations induced by megathrust earthquakes. This is consistent with studies suggesting a greater total moment released by crustal seismicity during of the coseismic interplate stage (Hardebeck, 2012; Hasegawa et al., 2012; Yoshida et al., 2012). Further, this is in agreement with the findings of Gombert et al. (2014), who conclude, from the analysis of the global CMT catalog (Dziewonski

Table 2

Parameters considered for the Mw and average slip estimates obtained for each fault considering the empirical relationships from (FILLIN "Thingbaijam et al., 2017).

Fault	LGF	LiF	PaF	NCF	ECF
Slip	Dextral	Dextral	Reverse	Normal	Normal
Length (km)	65	35	25	21	7.5
Rupture area (km ²)	780	420	300	252	900
Mw	6.8	6.5	6.5	6.1	5.5
Average Slip (m)	0.58	0.39	0.60	0.21	0.08

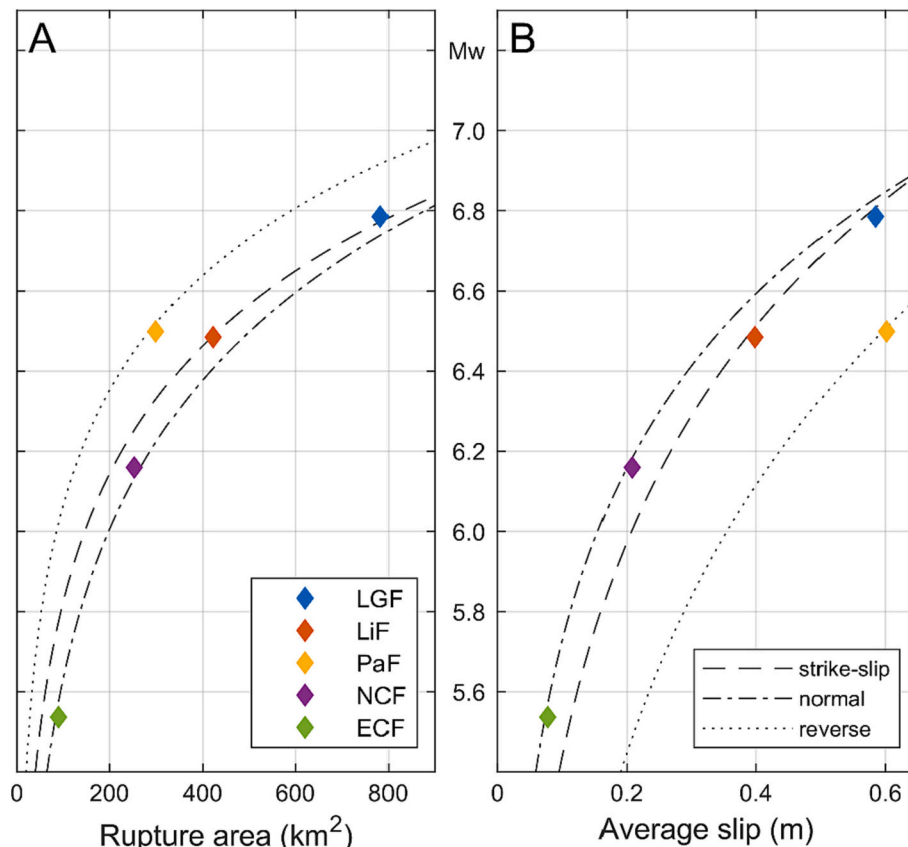


Fig. 11. Mw (A) and average slip (m)(B) estimations for earthquakes on the dextral (LGF and LiF), normal (NCF and ECF) and reverse (PaF) faults using the rupture area (km²) as input, according to the Thingbaijam et al. (2017) empirical relationships. Dotted, dashed and dash-dotted lines correspond to the regression for reverse, strike-slip and normal faults respectively.

et al., 1981; Ekström et al., 2012) and published reports for the 1960 M9.5 Valdivia and 1964 M9.2 Alaska earthquakes, that the rate of crustal earthquakes in the overriding plate increases days after $M > 8.6$ megathrust earthquakes, in an area encompassing $\pm 10^\circ$ of latitude and longitude with respect to the triggering event centroid. On the contrary, the evidence for crustal fault reactivation during the interseismic stage is much less abundant. A possible explanation for this scarce evidence deals with the fact that the instrumental record covers only a narrow time span for the interseismic stage; thus, only a small fraction of the crustal earthquakes occurring during this period may be detected (Aron et al., 2014).

For the LOFS, no moderate-to-large earthquakes have been confirmed shortly after the 1960 Valdivia Earthquake. Although this can be explained by the lack of data, it is important to highlight that strike-slip faults in other oblique margins have neither been triggered shortly after (weeks) great megathrust earthquakes. Indeed, these faults have been reactivated decades after the precedent megathrust mainshock. For instance, Pollitz and Sacks (1997), by calculating Coulomb failure stress on the causative Nojima Fault – a branch of the Median Tectonic Line (MTL) in Japan – conclude that the M 6.91995 Kobe Earthquake was enhanced by the occurrence of $M > 8$ megathrust earthquakes along the Nankai subduction zone during the 1940s. Likewise, Bufe (2006) suggests that the M 7.92022 Denali Earthquake, which occurred on the Denali Fault (DF), was partially triggered by stress perturbations due to the 1964 M 9.2 Alaska. Similarly, McCloskey et al. (2005) propose that the GSF in Indonesia – a fault that has produced >20 Mw > 6.5 earthquakes in the last 110 years (Hurukawa et al., 2014) – was strengthened to experience a M 7–7.5 earthquake due to the stress increments produced by the megathrust M 9.32004 Sumatra-Andaman Island Earthquake. Although no earthquakes of the proposed magnitudes have yet

occurred on the GSF, a M 6.2 earthquake took place on this structure on February 25th, 2022. With these data, we propose that LOFS and secondary fault strands, although significantly affected by coseismic Δ CFS, do not necessarily slip during megathrust earthquakes. Interseismic Δ CFS, although of less magnitude, may represent the perturbations required to trigger intra-arc faults in the area.

The fact that some of the studied faults (PaF and ECF) are not favored (Δ CFS $< +0.1$ bar; misfit $> 22.5^\circ$) to be reactivated by any of the two modeled scenarios opens three possibilities. First, their reactivation would be due to Δ CFS rises induced by megathrust earthquakes with slip distributions different from that of the Valdivia Earthquake. Second, their reactivation may be caused by postseismic stress changes. Even if they were not modeled in this paper, Ding and Lin (2014) propose that postseismic Δ CFS associated to the 1960 Valdivia Earthquake significantly increased in the rupture area and nearby regions. Indeed, these authors suggest that the subsequent 2010 Maule Earthquake was, at least partially, triggered by the 1960 Valdivia postseismic Δ CFS. Third, their reactivation is controlled by major crustal structures in the area, rather than the megathrust seismic cycle. For instance, an alternative source of deformation for the PaF could be the Mocha-Villarrica Fault Zone (MVZF in Fig. 1b), a major crustal-scale sinistral transpressive structure oblique to the andean chain (Melnick and Echter, 2006) which, according to Cembrano and Lara (2009), is not coupled with the dextral-transpressive stress field of the arc.

Despite the limitations of our Δ CFS modeling approach, it allows shedding light onto the interaction between the megathrust earthquake cycle and the potential occurrence of moderate-to-large earthquake on intra-arc faults in the Southern Chile subduction zone. Future studies may address the interaction between megathrust ruptures different from the Valdivia 1960 earthquake – for instance with stochastic modeling –

and intra-arc faults. Another step in this sense may consider the 1960 postseismic Δ CFS on the LOFS and spatially related faults.

6. Conclusions

We have reported and characterized field evidence of deformation in four areas of the Southern Chile intra-arc between 39°S and 40.5°S. Evidence consists in deflected channels and offset markers at the 10^{-1} – 10^2 m scale. Age constraints suggest that this evidence is younger than 14 ka. The characterized evidence allows considering five faults in the area as neotectonic structures; these are, from south to north, the NNE-striking dextral Los Guindos Fault (LGF), the NNE-striking dextral Liquiñe Fault (LiF), the NE-striking reverse Palguín Fault (PaF), the NNE-striking normal Northern Caburgua Fault (NCF), and the NW-striking Eastern Caburgua Fault (ECF).

The general seismogenic behavior of the LOFS allows considering that the herein characterized deformed markers are, at least partially, due to shallow earthquake ruptures. Considering the length of each of the neotectonic faults reported in this paper, besides the seismogenic depth for the area (12 km depth), we conclude that they can produce Mw 5.5 to Mw 6.8 earthquakes with coseismic slip ranging between 0.08 m to 0.58 m.

Stress perturbations induced both by the 1960 Valdivia Earthquake and the modeled interseismic period increase the Δ CFS on the herein reported faults. These stress changes may have augmented the possibility of having crustal earthquakes on faults of the study area and, in general, within the entire southern Chile intra-arc in the future.

We propose that the intra-arc faults addressed in this paper, and certainly others in the Southern Chile intra-arc, must be considered as significant sources of seismic hazard. Shallow earthquakes on them could result in severe damage for urban areas and industrial facilities located in the periphery of these faults.

Author credit statement

All the authors listed on the manuscript participated actively on the field work or in the other phases of the project.

Declaration of Competing Interest

The authors declare that they have no known competing financial interests or personal relationships that could have appeared to influence the work reported in this paper.

Data availability

Data will be made available on request.

Acknowledgements

This research was supported by the Millennium Nucleus “CYCLO: The Seismic Cycle Along Subduction Zones” (NCN19.167), Comisión Nacional de Investigación Científica y Tecnológica PhD grant 21181673. Research by Joaquín Cortés-Aranda is founded by the Fondecyt Iniciación project 1180509, project GEOF 03-2020 and Vicerrectoría de investigación de la Universidad de Concepción VRID 2021000383MUL. The authors thank Constanza Romero, Diego Molina, Ambrosio Vega and Diego Castillo for participating in field campaigns.

Appendix A. Supplementary data

Supplementary data to this article can be found online at <https://doi.org/10.1016/j.tecto.2022.229675>.

References

- Allen, C.R., 1965. Transcurrent faults in continental areas. *Philos. Trans. R. Soc. Lond. Ser. A Math. Phys. Sci.* 258 (1088).
- Angermann, D., Klotz, J., Reigber, C., 1999. Space-geodetic estimation of the Nazca–South America Euler vector. *Earth Planet. Sci. Lett.* 171 (3), 329–334. [https://doi.org/10.1016/S0012-821X\(99\)00173-9](https://doi.org/10.1016/S0012-821X(99)00173-9).
- Aron, F., Allmendinger, R.W., Cembrano, J., Yáñez, G., González, G., Yáñez, G., 2013. Permanent fore-arc extension and seismic segmentation: Insights from the 2010 Maule earthquake, Chile. *J. Geophys. Res. Solid Earth* 118 (2), 724–739. <https://doi.org/10.1029/2012JB009339>.
- Aron, F., Cembrano, J., Astudillo, F., Allmendinger, R.W., Arancibia, G., 2014. Constructing forearc architecture over megathrust seismic cycles: geological snapshots from the Maule earthquake region, Chile. *Bull. Geol. Soc. Am.* 127 (3–4), 464–479. <https://doi.org/10.1130/B31125.1>.
- Astudillo-Sotomayor, L., Jara-Muñoz, J., Melnick, D., Cortés-Aranda, J., Tassara, A., Strecker, M.R., 2021. Fast Holocene slip and localized strain along the Liquiñe-Ofqui strike-slip fault system, Chile. *Sci. Rep.* 11 (1), 1–10. <https://doi.org/10.1038/s41598-021-85036-5>.
- Bakun, W.H., 1999. Seismic activity of the San Francisco Bay region. *Bull. Seismol. Soc. Am.* 89 (3), 764–784.
- Bakun, W., Aagaard, B., Dost, B., et al., 2005. Implications for prediction and hazard assessment from the 2004 Parkfield earthquake. *Nature* 437, 969–974. <https://doi.org/10.1038/nature04067>.
- Barrientos, S.E., Ward, S.N., 1990. The 1960 Chile earthquake: inversion for slip distribution from surface deformation. *Geophys. J. Int.* 103 (3), 589–598. <https://doi.org/10.1111/j.1365-246X.1990.tb05673.x>.
- Barrientos, S.E., Acevedo-Ardnigui, P.S., Acevedo-Aranguiz, P.S., 1992. Seismological aspects of the 1988–1989 Lonquimay (Chile) volcanic eruption. *J. Volcanol. Geotherm. Res.* 53 (1–4), 73–87. [https://doi.org/10.1016/0377-0273\(92\)90075-O](https://doi.org/10.1016/0377-0273(92)90075-O).
- Bellier, O., Sébrier, M., Pramumijoyo, S., Beaudouin, T., Harjono, H., Bahar, I., Forni, O., 1997. Paleoseismicity and seismic hazard along the Great Sumatran fault (Indonesia). *J. Geodyn.* 24 (1–4), 169–183. [https://doi.org/10.1016/S0264-3707\(96\)00051-8](https://doi.org/10.1016/S0264-3707(96)00051-8).
- Bonali, F.L., Tibaldi, A., Corazzato, C., Tormey, D.R., Lara, L.E., 2013. Quantifying the effect of large earthquakes in promoting eruptions due to stress changes on magma pathway: the Chile case. *Tectonophysics* 583, 54–67. <https://doi.org/10.1016/j.tecto.2012.10.025>.
- Bucchi, F., Lara, L.E., Gutiérrez, F., 2015. The Carrán-Los Venados volcanic field and its relationship with coeval and nearby polygenetic volcanism in an intra-arc setting. *J. Volcanol. Geotherm. Res.* 308, 70–81. <https://doi.org/10.1016/j.jvolgeores.2015.10.013>.
- Bufe, C.G., 2006. Coulomb stress transfer and tectonic loading preceding the 2002 Denali fault earthquake. *Bull. Seismol. Soc. Am.* 96 (5), 1662–1674. <https://doi.org/10.1785/0120050007>.
- Campos, A., Moreno, H., Muñoz, J., Antinao, J.L., Clayton, J., Martin, M., 1998. Area de Futrono-Lago Ranco, Región de Los Lagos. In: *Servicio Nacional de Geología y Minería, Mapas Geológicos No. 8, escala 1:100.000*. Santiago.
- Cembrano, J., Lara, L., 2009. The link between volcanism and tectonics in the southern volcanic zone of the Chilean Andes: a review. *Tectonophysics* 471 (1–2), 96–113. <https://doi.org/10.1016/j.tecto.2009.02.038>.
- Cembrano, J., Hervé, F., Lavenue, A., 1996. The Liquiñe Ofqui fault zone: a long-lived intra-arc fault system in southern Chile. *Tectonophysics* 259 (1–3 SPEC. ISS), 55–66. [https://doi.org/10.1016/0040-1951\(95\)00066-6](https://doi.org/10.1016/0040-1951(95)00066-6).
- Cembrano, J., Schermer, E., Lavenue, A., Sanhueza, A., 2000. Contrasting nature of deformation along an intra-arc shear zone, the Liquiñe-Ofqui fault zone, southern Chilean Andes. *Tectonophysics* 319. <http://www.elsevier.com/locate/tecto>.
- Cembrano, J., Lavenue, A., Reynolds, P., Arancibia, G., López, G., Sanhueza, A., 2002. Late Cenozoic transpressional ductile deformation north of the Nazca–South America–Antarctica triple junction. *Tectonophysics* 354 (3–4). [https://doi.org/10.1016/S0040-1951\(02\)00388-8](https://doi.org/10.1016/S0040-1951(02)00388-8).
- Chaussard, E., Bürgmann, R., Fattahi, H., Johnson, C.W., Nadeau, R., Taira, T., Johanson, I., 2015. Interseismic coupling and refined earthquake potential on the Hayward–Calaveras fault zone. *J. Geophys. Res. Solid Earth* 120 (12), 8570–8590. <https://doi.org/10.1002/2015JB012230>.
- Chinn, D.S., Isacks, B.L., 1983. Accurate source depths and focal mechanisms of shallow earthquakes in western South America and in the New Hebrides Island Arc. *Tectonics* 2 (6), 529–563. <https://doi.org/10.1029/TC002i006p00529>.
- Cisternas, M., Atwater, B.F., Torrejón, F., Sawai, Y., Machuca, G., Lagos, M., Eipert, A., Youton, C., Salgado, I., Kamataki, T., Shishikura, M., Rajendran, C.P., Malik, J.K., Rizal, Y., Husni, M., 2005. Predecessors of the giant 1960 Chile earthquake. *Nature* 437 (7057), 404–407. <https://doi.org/10.1038/nature03943>.
- Colavitto, B., Sagripanti, L., Jagoe, L., Costa, C., Folguera, A., 2020. Quaternary tectonics in the southern Central Andes (37°–38° S): Retroarc compression inferred from morphotectonics and numerical models. *J. S. Am. Earth Sci.* 102 (June), 102697. <https://doi.org/10.1016/j.jsames.2020.102697>.
- Cortés-Aranda, J., González, G., Rémy, D., Martinod, J., 2015. Normal upper plate fault reactivation in northern Chile and the subduction earthquake cycle: from geological observations and static Coulomb Failure Stress (CFS) change. *Tectonophysics* 639, 118–131. <https://doi.org/10.1016/j.tecto.2014.11.019>.
- De Pascale, G.P., Froude, M., Penna, I., Hermanns, R.L., Sepúlveda, S.A., Moncada, D., Persico, M., Easton, G., Villalobos, A., Gutiérrez, F., 2021. Liquiñe-Ofqui’s fast slipping intra-volcanic arc crustal faulting above the subducted Chile Ridge. *Sci. Rep.* 11 (1), 7069. <https://doi.org/10.1038/s41598-021-86413-w>.

- Dieterich, J., 1994. A constitutive law for rate of earthquake production and its application to earthquake clustering. *J. Geophys. Res. Solid Earth* 99 (B2), 2601–2618. <https://doi.org/10.1029/93JB02581>.
- Ding, M., Lin, J., 2014. Post-seismic viscoelastic deformation and stress transfer after the 1960 M9.5 Valdivia, Chile earthquake: effects on the 2010 M8.8 Maule, Chile earthquake. *Geophys. J. Int.* 197, 697–704. <https://doi.org/10.1093/gji/ggu048>.
- Douillet, G.A., Taisne, B., Tsang-Hin-Sun, E., Müller, S.K., Kueppers, U., Dingwell, D.B., 2015. Syn-eruptive, soft-sediment deformation of deposits from dilute pyroclastic density current: Triggers from granular shear, dynamic pore pressure, ballistic impacts and shock waves. *Solid Earth* 6 (2), 553–572. <https://doi.org/10.5194/SE-6-553-2015>.
- Dziwowski, A.M., Chou, T.A., Woodhouse, J.H., 1981. Determination of earthquake source parameters from waveform data for studies of global and regional seismicity. *J. Geophys. Res. Solid Earth* 86 (B4), 2825–2852. <https://doi.org/10.1029/JB086IB04P02825>.
- Ekmström, G., Nettles, M., Dziwowski, A.M., 2012. The global CMT project 2004–2010: Centroid-moment tensors for 13,017 earthquakes. *Phys. Earth Planet. Inter.* 200–201, 1–9. <https://doi.org/10.1016/J.PEPI.2012.04.002>.
- Fariás, M., Comte, D., Roecker, S., Carrizo, D., Pardo, M., 2011. Crustal extensional faulting triggered by the 2010 Chilean earthquake: the Pichilemu Seismic Sequence. *Tectonics* 30 (6). <https://doi.org/10.1029/2011TC002888>.
- Fitch, T.J., 1972. Plate convergence, transcurent faults, and internal deformation adjacent to Southeast Asia and the western Pacific. *J. Geophys. Res.* 77 (23), 4432–4460. <https://doi.org/10.1029/jb077i023p04432>.
- Folguera, A., Ramos, V.A., Hermanns, R.L., Naranjo, J., 2004. Neotectonics in the foothills of the southernmost central Andes (37°–38°S): evidence of strike-slip displacement along the Antinir-Copahue fault zone. *Tectonics* 23 (5). <https://doi.org/10.1029/2003TC001533>.
- Forsythe, R., Nelson, E., 1985. Geological manifestations of ridge collision: evidence from the Golfo de Penas-Taitao Basin, southern Chile. *Tectonics* 4 (5), 477–495. <https://doi.org/10.1029/TC004i005p0477>.
- Fuji, Y., Satake, K., 2013. Slip distribution and seismic moment of the 2010 and 1960 Chilean Earthquakes inferred from Tsunami waveforms and coastal geodetic data. *Pure Appl. Geophys.* 170 (9–10), 1493–1509. <https://doi.org/10.1007/s00024-012-0524-2>.
- Gomberg, J., Sherrod, B., Gomberg, J., 2014. Crustal earthquake triggering by modern great earthquakes on subduction zone thrusts. *J. Geophys. Res. Solid Earth* 119 (2), 1235–1250. <https://doi.org/10.1002/2012JB009826>.
- Guzmán-Marín, P., Lira, M.P., Tassara, A., Urrutia, R., 2015. Nuevos antecedentes tectónicos del Sistema de Fallas Liquiñe-Ofqui en la Cuenca de Intra-arco del Lago Maihue (40° 16'S 72°W), Andes del Sur, Chile. In: *XIV Congreso Geológico Chileno, August*, 40–43.
- Haberland, C., Rietbrock, A., Lange, D., Bataille, K., Hofmann, S., 2006. Interaction between forearc and oceanic plate at the south-central Chilean margin as seen in local seismic data. *Geophys. Res. Lett.* 33 (23). <https://doi.org/10.1029/2006GL028189>.
- Hardebeck, J.L., 2012. Coseismic and postseismic stress rotations due to great subduction zone earthquakes. *Geophys. Res. Lett.* 39 (21), 21313. <https://doi.org/10.1029/2012GL053438>.
- Harris, R.A., 2017. Large earthquakes and creeping faults. *Rev. Geophys.* 55 (1), 169–198. <https://doi.org/10.1002/2016RG000539>.
- Hasegawa, A., Yoshida, K., Asano, Y., Okada, T., Inuma, T., Ito, Y., 2012. Change in stress field after the 2011 great Tohoku-Oki earthquake. *Earth Planet. Sci. Lett.* 355–356, 231–243. <https://doi.org/10.1016/j.epsl.2012.08.042>.
- Hernández-Moreno, C., Speranza, F., Di Chiara, A., 2014. Understanding kinematics of intra-arc transcurent deformation: Paleomagnetic evidence from the Liquiñe-Ofqui fault zone (Chile, 38–41S). *Tectonics* 33 (10), 1964–1988. <https://doi.org/10.1002/2014TC003622>.
- Hurukawa, N., Wulandari, B.R., Kasahara, M., 2014. Earthquake history of the Sumatran fault, Indonesia, since 1892, derived from relocation of large earthquakes. *Bull. Seismol. Soc. Am.* 104 (4), 1750–1762. <https://doi.org/10.1785/0120130201>.
- Ito, T., Gunawan, E., Kimata, F., Tabei, T., Simons, M., Meilano, I., Agustan, N., Ohta, Y., Nurdin, I., Sugiyanto, D., 2012. Isolating along-strike variations in the depth extent of shallow creep and fault locking on the northern Great Sumatran Fault. *J. Geophys. Res. Solid Earth* 117 (6), 1–16. <https://doi.org/10.1029/2011JB008940>.
- Iturrieta, P.C., Hurtado, D.E., Cembrano, J., Stanton-Yonge, A., 2017. States of stress and slip partitioning in a continental scale strike-slip duplex: Tectonic and magmatic implications by means of finite element modeling. *Earth Planet. Sci. Lett.* 473, 71–82. <https://doi.org/10.1016/j.epsl.2017.05.041>.
- Jagoe, L., Sargipanti, L., Colavito, B., Folguera, A., 2021. Landscape evolution in the Guanacos fold and thrust belt (37° S): Insights from geomorphological and morphometric analysis. *J. S. Am. Earth Sci.* 111 (July), 103484. <https://doi.org/10.1016/j.jsames.2021.103484>.
- Jarrard, R.D., 1986. Terrane motion by strike-slip faulting of forearc slivers. *Geology* 14 (9), 780–783. [https://doi.org/10.1130/0091-7613\(1986\)14<780:TMSFO>2.0.CO;2](https://doi.org/10.1130/0091-7613(1986)14<780:TMSFO>2.0.CO;2).
- Johanson, I., 2006. Slip Characteristics of San Andreas Fault Transition Zone Segments. <http://citeseerx.ist.psu.edu/viewdoc/download?doi=10.1.1.663.3300&rep=rep1&type=pdf>.
- Kendrick, E.C., Bevis, M., Smalley, R.F., Cifuentes, O., Galban, F., 1999. Current rates of convergence across the Central Andes : estimates from continuous GPS observations. *Geophys. Res. Lett.* 26 (5), 541–544. <https://doi.org/10.1029/1999GL000040>.
- Kendrick, E., Bevis, M., Smalley Jr., R., Brooks, B., Vargas, R.B., Lauria, E., Fortes, L.P.S., 2003. The Nazca–South America Euler vector and its rate of change. *J. S. Am. Earth Sci.* 16 (2), 125–131.
- Khazaradze, G., Wang, K., Klotz, J., Hu, Y., He, J., 2002. Prolonged post-seismic deformation of the 1960 great Chile earthquake and implications for mantle rheology. *Geophys. Res. Lett.* 29 (22), 7–1–7–4. <https://doi.org/10.1029/2002GL015986>.
- Lange, D., Cembrano, J., Rietbrock, A., Haberland, C., Dahm, T., Bataille, K., 2008. First seismic record for intra-arc strike-slip tectonics along the Liquiñe-Ofqui fault zone at the obliquely convergent plate margin of the southern Andes. *Tectonophysics* 455 (1–4), 14–24. <https://doi.org/10.1016/j.tecto.2008.04.014>.
- Lange, D., Ruiz, J., Carrasco, S., Manríquez, P., 2018. The Chiloe Mw 7.6 earthquake of 2016 december 25 in southern Chile and its relation to the Mw 9.5 1960 Valdivia earthquake. *Geophys. J. Int.* 213 (1), 210–221. <https://doi.org/10.1093/gji/ggx514>.
- Lara, L., Moreno, H., Roa, H., 2004. Geología del Área Liquiñe-Neltume, Regiones de La Araucanía y de Los Lagos. In: *Servicio Nacional de Geología y Minería, Carta Geológica de Chile, Serie Geología Básica*, 83, 23p., 1 mapa escala 1:100.000, p. 1 Map.
- Lara, L.E., Lavenue, A., Cembrano, J., Rodríguez, C., 2006. Structural controls of volcanism in transversal chains: resheared faults and neotectonics in the Cordón Caulle-Puyehue area (40.5°S), Southern Andes. *J. Volcanol. Geotherm. Res.* 158 (1–2), 70–86. <https://doi.org/10.1016/j.jvolgeores.2006.04.017>.
- Lara, L.E., Cembrano, J., Lavenue, A., 2008. Quaternary vertical displacement along the liquiñe-Ofqui fault zone: differential uplift and coeval volcanism in the Southern Andes? *Int. Geol. Rev.* 50 (11), 975–993. <https://doi.org/10.2747/0020-6814.50.11.975>.
- Lavenue, A., Cembrano, J., 1999. Compression-and transpression-stress pattern for Pliocene and Quaternary brittle deformation in fore arc and intra-arc zones (Andes of Central and Southern Chile). *J. Struct. Geol.* 21 (12). [https://doi.org/10.1016/S0191-8141\(99\)00111-X](https://doi.org/10.1016/S0191-8141(99)00111-X). Pergamon.
- Legrand, D., Barrientos, S., Bataille, K., Cembrano, J., Pavez, A., 2011. The fluid-driven tectonic swarm of Aysen Fjord, Chile (2007) associated with two earthquakes (Mw=6.1 and Mw=6.2) within the Liquiñe-Ofqui Fault Zone. *Cont. Shelf Res.* 31 (3–4), 154–161. <https://doi.org/10.1016/j.csr.2010.05.008>.
- Lomnitz, C., 2004. Major earthquakes of Chile: a historical survey, 1535–1960. *Seismol. Res. Lett.* 75 (3), 368–378. <https://doi.org/10.1785/gssrl.75.3.368>.
- Loveless, J.P., Allmendinger, R.W., Pritchard, M.E., González, G., 2010. Normal and reverse faulting driven by the subduction zone earthquake cycle in the northern Chilean fore arc. *Tectonics* 29 (2), 1–16. <https://doi.org/10.1029/2009TC002465>.
- Lupi, M., Miller, S.A., 2014. Short-lived tectonic switch mechanism for long-term pulses of volcanic activity after mega-thrust earthquakes. *Solid Earth* 5 (1), 13–24. <https://doi.org/10.5194/se-5-13-2014>.
- Maldonado, V., Contreras, M., Melnick, D., 2021. A comprehensive database of active and potentially-active continental faults in Chile at 1:25,000 scale. *Sci. Data* 8 (1), 20. <https://doi.org/10.1038/s41597-021-00802-4>.
- Maloney, K.T., Clarke, G.L., Klepeis, K.A., Quevedo, L., 2013. The Late Jurassic to present evolution of the Andean margin: drivers and the geological record. *Tectonics* 32 (5), 1049–1065. <https://doi.org/10.1002/tect.20067>.
- McCalpin, J. P. (2009). Paleoseismology.
- McCloskey, J., Nalbant, S.S., Steacy, S., 2005. Earthquake risk from co-seismic stress. *Nature* 434 (7031), 291. <https://doi.org/10.1038/434291a>.
- Melnick, D., Echter, H.P., 2006. Inversion of forearc basins in south-central Chile caused by rapid glacial age trench fill. *Geology* 34 (9), 709–712. <https://doi.org/10.1130/G22440.1>.
- Melnick, D., Folguera, A., Ramos, V.A., 2006a. Structural control on arc volcanism: the Cavihue-Copahue complex, Central to Patagonian Andes transition (38°S). *J. S. Am. Earth Sci.* 22 (1–2), 66–88. <https://doi.org/10.1016/j.jsames.2006.08.008>.
- Melnick, D., Rosenau, M., Folguera, A., Echter, H., 2006b. Neogene tectonic evolution of the Neuquén Andes western flank (37–39°S). *Spec. Pap. Geol. Soc. Am.* 407, 73–95. [https://doi.org/10.1130/2006.2407\(04\)](https://doi.org/10.1130/2006.2407(04)).
- Melnick, D., Bookhagen, B., Strecker, M.R., Echter, H.P., 2009. Segmentation of megathrust rupture zones from fore-arc deformation patterns over hundreds to millions of years, Arauco peninsula, Chile. *J. Geophys. Res. Solid Earth* 114 (1). <https://doi.org/10.1029/2008JB005788>.
- Melnick, D., Li, S., Moreno, M., Cisternas, M., Jara-Muñoz, J., Wesson, R., Nelson, A., Báez, J.C., Deng, Z., 2018. Back to full interseismic plate locking decades after the giant 1960 Chile earthquake. *Nat. Commun.* 9 (1), 3527. <https://doi.org/10.1038/s41467-018-05989-6>.
- Mitogawa, T., Nishimura, T., 2020. Coulomb stress change on inland faults during megathrust earthquake cycle in southwest Japan. *Earth Planet. Space*. <https://doi.org/10.1186/s40623-020-01174-6>.
- Moreno Roa, H., Lara, L.E., 2008. Geología del Área Pucón-Curruhue, Regiones de La Araucanía y de Los Ríos. In: *Servicio Nacional de Geología y Minería, Carta Geológica de Chile, Serie Geología Básica* 115: 36 p., 1 mapa escala 1:100.000.
- Moreno, M.S., Bolte, J., Klotz, J., Melnick, D., 2009. Impact of megathrust geometry on inversion of coseismic slip from geodetic data: application to the 1960 Chile earthquake. *Geophys. Res. Lett.* 36 (16), L16310. <https://doi.org/10.1029/2009GL039276>.
- Moreno, M., Melnick, D., Rosenau, M., Bolte, J., Klotz, J., Echter, H., Baez, J., Bataille, K., Chen, J., Bevis, M., Hase, H., Oncken, O., 2011. Heterogeneous plate locking in the South-Central Chile subduction zone: Building up the next great earthquake. *Earth Planet. Sci. Lett.* 305 (3–4), 413–424. <https://doi.org/10.1016/j.epsl.2011.03.025>.
- Moreno, M., Li, S., Melnick, D., Bedford, J.R., Baez, J.C., Motagh, M., Metzger, S., Vajedian, S., Sippl, C., Gutknecht, B.D., Contreras-Reyes, E., Deng, Z., Tassara, A., Oncken, O., 2018. Chilean megathrust earthquake recurrence linked to frictional contrast at depth. *Nat. Geosci.* 11 (4), 285–290. <https://doi.org/10.1038/s41561-018-0089-5>.

- Muksin, U., Bauer, K., Muzli, M., Ryberg, T., Nurdin, I., Masturiyono, M., Weber, M., 2019. AcehSeis project provides insights into the detailed seismicity distribution and relation to fault structures in Central Aceh, Northern Sumatra. *J. Asian Earth Sci.* 171, 20–27. <https://doi.org/10.1016/j.jseas.2018.11.002>.
- Nakano, M., Kumagai, H., Toda, S., Ando, R., Yamashina, T., Inoue, H., Sunarjo, T., 2010. Source model of an earthquake doublet that occurred in a pull-apart basin along the Sumatran fault, Indonesia. *Geophys. J. Int.* 181 (1), 141–153. <https://doi.org/10.1111/j.1365-246X.2010.04511.x>.
- Oppenheimer, D.H., Bakun, W.H., Parsons, T., Simpson, R.W., Boatwright, J., Uhrhammer, R.A., 2010. The 2007 M5.4 Alum Rock, California, earthquake: implications for future earthquakes on the central and southern Calaveras Fault. *J. Geophys. Res. Solid Earth* 115 (B8). <https://doi.org/10.1029/2009JB006683>.
- Pardo-Casas, F., Molnar, P., 1987. Relative motion of the Nazca (Farallon) and South American plates since late cretaceous time. *Tectonics* 6 (3).
- Peña, C., Cabello, C., Tassara, A., 2021. Dynamic and kinematic characterization of the basement structures of the Mocho-Choshuencho Volcanic Complex, Southern Andes, Chile. *J. S. Am. Earth Sci.* 111 (June), 103435. <https://doi.org/10.1016/j.jsames.2021.103435>.
- Pérez-Estay, N., Yáñez, G., Crempien, J., Roquer, T., Cembrano, J., Valdenegro, P., Aravena, D., Arancibia, G., Morata, D., 2020. Seismicity in a transpressional volcanic arc: the Liquiñe-Ofqui Fault System in the Puyuhuapi Area, Southern Andes, Chile (44°S). *Tectonics* 39 (11), 1–26. <https://doi.org/10.1029/2020TC006391>.
- Pérez-Flores, P., Cembrano, J., Sánchez-Alfaro, P., Veloso, E., Arancibia, G., Roquer, T., 2016. Tectonics, magmatism and paleo-fluid distribution in a strike-slip setting: insights from the northern termination of the Liquiñe-Ofqui fault system, Chile. *Tectonophysics* 680, 192–210. <https://doi.org/10.1016/j.tecto.2016.05.016>.
- Pérez-Flores, P., Veloso, E., Cembrano, J., Sánchez-Alfaro, P., Lizama, M., Arancibia, G., 2017. Fracture network, fluid pathways and paleostress at the Tolhuaca geothermal field. *J. Struct. Geol.* 96, 134–148. <https://doi.org/10.1016/j.jsg.2017.01.009>.
- Pollitz, F.F., Sacks, I.S., 1997. The 1995 Kobe, Japan, earthquake: a long-delayed aftershock of the offshore 1944 Tonankai and 1946 Nankaido earthquakes. *Bull. Seismol. Soc. Am.* 87 (1), 1–10. <https://doi.org/10.1785/BSSA0870010001>.
- Quiero, F., Tassara, A., Iaffaldano, G., Rabbia, O., 2022. Growth of Neogene Andes linked to changes in plate convergence using high-resolution kinematic models. *Nat. Commun.* 13 (1), 1–9. <https://doi.org/10.1038/s41467-022-29055-4>.
- Radice, J.P., 2010. The Cenozoic basins and their control on volcanism of Chillan and Callaqui-Copahue complexes (36–39°S Southern Andes). *Andean Geol.* 37 (1), 220–246.
- Rawson, H., Naranjo, J.A., Smith, V.C., Fontijn, K., Pyle, D.M., Mather, T.A., Moreno, H., 2015. The frequency and magnitude of post-glacial explosive eruptions at Volcán Mocho-Choshuencho, southern Chile. *J. Volcanol. Geotherm. Res.* 299, 103–129. <https://doi.org/10.1016/j.jvolgeores.2015.04.003>.
- Rosenau, M., Melnick, D., Echter, H., 2006. Kinematic constraints on intra-arc shear and strain partitioning in the southern Andes between 38°S and 42°S latitude. *Tectonics* 25 (4). <https://doi.org/10.1029/2005TC001943>.
- Russo, R.M., Gallego, A., Comte, D., Mocanu, V.I., Mordie, R.E., Mora, C., VanDecar, J.C., 2011. Triggered seismic activity in the Liquiñe-Ofqui fault zone, southern Chile, during the 2007 Aysen seismic swarm. *Geophys. J. Int.* 184 (3), 1317–1326. <https://doi.org/10.1111/j.1365-246X.2010.04908.x>.
- Sánchez, P., Pérez-Flores, P., Arancibia, G., Cembrano, J., Reich, M., 2013. Crustal deformation effects on the chemical evolution of geothermal systems: the intra-arc Liquiñe-Ofqui fault system, Southern Andes. *Int. Geol. Rev.* 55 (11), 1384–1400. <https://doi.org/10.1080/00206814.2013.775731>.
- Savage, J.C., 1983. A dislocation model of strain accumulation and release at a subduction zone. *J. Geophys. Res. Solid Earth* 88 (B6), 4984–4996. <https://doi.org/10.1029/JB088iB06p04984>.
- Scholz, C.H., 1998. Earthquakes and friction laws. *Nature* 391 (6662), 37–42. <https://doi.org/10.1038/34097>.
- Sgambato, C., Faure Walker, J.P., Mildon, Z.K., Roberts, G.P., 2020. Stress loading history of earthquake faults influenced by fault/shear zone geometry and Coulomb pre-stress. *Sci. Rep.* 10 (1), 1–10. <https://doi.org/10.1038/s41598-020-69681-w>.
- Sielfeld, G., Cembrano, J., Lara, L., 2017. Transtension driving volcano-edifice anatomy: Insights from Andean transverse-to-the-orogen tectonic domains. *Quat. Int.* 438, 33–49. <https://doi.org/10.1016/j.quaint.2016.01.002>.
- Sielfeld, G., Lange, D., Cembrano, J., 2019. Intra-Arc Crustal Seismicity: Seismotectonic Implications for the Southern Andes Volcanic Zone, Chile. *Tectonics* 38 (2), 552–578. <https://doi.org/10.1029/2018TC004985>.
- Slemmons, D.B., dePollo, C.M., 1986. Evaluation of active faulting and associated hazard. In: 1986 National Academies Press (Ed.) (Ed.), *Active Tectonics*, 1st ed. pp. 45–62. <https://www.nap.edu/read/624/chapter/5>.
- Stanton-Yonge, A., Griffith, W.A., Cembrano, J., St. Julien, R., Iturrieta, P., 2016. Tectonic role of margin-parallel and margin-transverse faults during oblique subduction in the Southern Volcanic Zone of the Andes: insights from Boundary Element Modeling. *Tectonics* 35 (9), 1990–2013. <https://doi.org/10.1002/2016TC004226>.
- Tardani, D., Reich, M., Roulleau, E., Takahata, N., Sano, Y., Pérez-Flores, P., Sánchez-Alfaro, P., Cembrano, J., Arancibia, G., 2016. Exploring the structural controls on helium, nitrogen and carbon isotope signatures in hydrothermal fluids along an intra-arc fault system. *Geochim. Cosmochim. Acta* 184, 193–211. <https://doi.org/10.1016/j.gca.2016.04.031>.
- Thingbaijam, K.K.S., Mai, P.M., Goda, K., 2017. New empirical earthquake source-scaling laws. *Bull. Seismol. Soc. Am.* 107 (5), 2225–2246. <https://doi.org/10.1785/0120170017>.
- Toda, S., Stein, R., 2003. Toggling of seismicity by the 1997 Kagoshima earthquake couplet: a demonstration of time-dependent stress transfer. *J. Geophys. Res. Solid Earth* 108 (B12). <https://doi.org/10.1029/2003JB002527>.
- Toda, S., Stein, R.S., Sevilgen, V., Lin, J., 2011. Coulomb 3.3 Graphic-rich deformation and stress-change software for earthquake, tectonic, and volcano research and teaching-user guide. In: Open-File Report. <https://doi.org/10.3133/ofr20111060>.
- Tong, X., Sandwell, D.T., Schmidt, D.A., 2018. Surface creep rate and moment accumulation rate along the Aceh segment of the Sumatran Fault from L-band ALOS-1/PALSAR-1 observations. *Geophys. Res. Lett.* 45 (8), 3404–3412. <https://doi.org/10.1002/2017GL076723>.
- Valentine, G.A., Fierstein, J., White, J.D.L., 2021. Soft sediment deformation in dry pyroclastic deposits at Ubehebe Crater, Death Valley. *Calif. Geol.* 49 (2), 211–215. <https://doi.org/10.1130/G48147.1>.
- Vargas Easton, G., Rebollo, S., Sepúlveda, S.A., Lahsen, A., Thiele, R., Townley, B., Padilla, C., Rauld, R., Herrera, M.J., Lara, M., 2013. Submarine earthquake rupture, active faulting and volcanism along the major Liquiñe-Ofqui Fault Zone and implications for seismic hazard assessment in the Patagonian Andes. *Andean Geol.* 40 (1), 141–171. <https://doi.org/10.5027/andgeov40n1-a07>.
- Villalobos, A., Vargas Easton, G., Maksymowicz, A., Ruiz, S., Lastras, G., De Pascale, G.P., Agurto-Detzel, H., 2020. Active faulting, submarine surface rupture and seismic migration along the Liquiñe-Ofqui fault system, Patagonian Andes. *J. Geophys. Res. Solid Earth*. <https://doi.org/10.1029/2020JB019946>.
- Wang, K., Hu, Y., Bevis, M., Kendrick, E., Robert, S., Vargas, R.B., Lauria, E., 2007. Crustal motion in the zone of the 1960 Chile earthquake: detangling earthquake-cycle deformation and forearc-silver translation. *Geochim. Geophys. Geosyst.* 8 (10). <https://doi.org/10.1029/2007GC001721>.
- Wils, K., Van Daele, M., Lastras, G., Kissel, C., Lamy, F., Siani, G., 2018. Holocene event record of Aysén Fjord (Chilean Patagonia): an interplay of volcanic eruptions and crustal and megathrust earthquakes. *J. Geophys. Res. Solid Earth* 123 (1), 324–343. <https://doi.org/10.1002/2017JB014573>.
- Wils, K., Van Daele, M., Kissel, C., Moernaut, J., Schmidt, S., Siani, G., Lastras, G., 2020. Seismo-turbidites in Aysén Fjord (Southern Chile) reveal a complex pattern of rupture modes along the 1960 megathrust earthquake segment. *J. Geophys. Res. Solid Earth*. <https://doi.org/10.1029/2020JB019405>.
- Yoshida, K., Hasegawa, A., Okada, T., Inuma, T., Ito, Y., Asano, Y., 2012. Stress before and after the 2011 great Tohoku-oki earthquake and induced earthquakes in inland areas of eastern Japan. *Geophys. Res. Lett.* <https://doi.org/10.1029/2011GL049729>.
- Zielke, O., Arrowsmith, J.R., 2012. LaDiCaoz and LiDARimager-MATLAB GUIs for LiDAR data handling and lateral displacement measurement. *Geosphere* 8 (1), 206–221. <https://doi.org/10.1130/GES00686.1>.